APPLIED PHYSICS REVIEWS

Rare-earth doped polymers for planar optical amplifiers

L. H. Slooff,[a] A. van Blaaderen, and A. Polman
FOM Institute for Atomic and Molecular Physics, Kruislaan 407, 1098 SJ Amsterdam, The Netherlands

G. A. Hebbink, S. I. Klink, F. C. J. M. Van Veggel, and D. N. Reinhoudt
Supramolecular Chemistry and Technology, University of Twente, P.O. Box 217, 7500 AE Enschede, The Netherlands

J. W. Hofstraat
Philips Research, Department of Polymers and Organic Chemistry, Prof. Holstlaan 4, 5656 AA Eindhoven, The Netherlands

(Received 6 August 2001; accepted for publication 14 December 2001)

Optical waveguide amplifiers based on polymer materials offer a low-cost alternative for inorganic waveguide amplifiers. Due to the fact that their refractive index is similar to that of standard optical fibers, they can be easily coupled to existing fibers with low coupling losses. Doping the polymer with rare-earth ions that yield optical gain is not straightforward, as the rare-earth salts are poorly soluble in the polymer matrix. This review article focuses on two different approaches to dope a polymer waveguide with rare-earth ions. The first approach is based on organic cage-like complexes that encapsulate the rare-earth ion and are designed to provide coordination sites to bind the rare-earth ion and to shield it from the surrounding matrix. These complexes also offer the possibility of attaching a highly absorbing antenna group, which increases the pump efficiency significantly. The second approach to fabricate rare-earth doped polymer waveguides is obtained by combining the excellent properties of SiO_2 as a host for rare-earth ions with the easy processing of polymers. This is done by doping polymers with Er-doped silica colloidal spheres. © *2002 American Institute of Physics.* [DOI: 10.1063/1.1454190]

I. INTRODUCTION

A. General introduction

In optical telecommunication systems, light is used to transport information between different users. To manipulate the optical signals on a local scale, devices like splitters, couplers, multiplexers, demultiplexers, and amplifiers are needed. Such devices can be readily made and integrated on one planar substrate, a technology called integrated optics. A basic element of a photonic integrated circuit is the planar optical waveguide. It consists of a high refractive index guiding layer, sandwiched between two lower-index cladding layers. The optical signal travels in the guiding layer and is confined in the transverse directions as a result of total internal reflection at the interfaces between core and cladding.

Optical (absorption and scattering) losses in the waveguide, coupling losses, or intrinsic intensity losses in optical splitters, call for the integration of optical amplifiers with waveguides and other components in photonic integrated circuits. These can be made by doping the guiding layer with an active element that (if pumped properly) gives rise to the optical gain. This review article will discuss the optical properties of polymer optical materials doped with rare-earth ions as the active element, that can be used for optical amplication.

Trivalent rare-earth ions such as erbium (Er), neodymium (Nd), europium (Eu), and terbium (Tb) are well known for their special optical properties, which result from the fact that the electrons of the partially filled $4f$ shell are shielded from the surrounding completely filled $5s$ and $5p$ shells. The energy levels of the $4f$ shell have equal parity, and hence electric dipole transitions are forbidden. In a solid, the small mixing with odd-parity wave functions makes the transition slightly allowed. The absorption and emission cross sections are therefore small, and the luminescence lifetimes can be quite long (ms). The influence of the electric field around the ion removes the degeneracy of the $4f$ levels, resulting in a Stark-splitting of the energy levels. However, due to the shielding by the outer lying shells, the magnitude of the splitting is small, resulting in relatively narrow emission lines, of which the wavelength is almost independent of the host material. For telecommunication applications, the rare-earth ions Er and Nd are used as they have transitions at 1.53 μm and 1.34 μm, respectively, which are two standard wavelengths used in telecommunication.

In order to achieve optical gain using these rare-earth ions, the ion is first excited from the ground state into a higher-lying state. From there, it can decay to the luminescent state from which it can return to a lower-lying state by

[a]Electronic mail: slooff@ecn.nl

emission of a photon. If the pump rate is high enough, population inversion between the two levels involved in the emission builds up. A telecommunication signal can then induce stimulated emission in the rare-earth ion resulting in amplification of the signal.

As already mentioned, the choice of host material in rare-earth doped optical waveguide amplifiers hardly influences the energy levels of the rare-earth ions. Therefore, in principle, any material that has little absorption at the pump and emission wavelengths can be used. Many different rare-earth doped inorganic materials have been studied, e.g., pure SiO_2, silicate and phosphate glasses, $LiNbO_3$, and Al_2O_3.[1] In some cases, optical gain has been achieved. Only recently, the use of polymers in optical waveguide amplifiers is being considered.[2]

The growing interest in polymers for use in integrated optics stems from the potential of mass production of low-cost devices on planar substrates, combined with the wide range of optical properties available for specific applications. Polymers developed for use in optical telecommunication applications include acrylates, polyimides, and olefins. The refractive index of these polymers can be tuned with an accuracy of less than 0.0001 by blending and co-polymerization.[3]

Low optical absorption is one of the major requirements for the host material. In polymers, optical absorption is caused by both molecular or polymeric electronic excited states, and by fundamental and overtone vibrations of molecular bonds. The most important absorption in the optical telecommunication window around 1.5 μm is due to vibrational states of O—H and C—H bonds. Since the energy of the vibration is inversely related to the reduced mass, substitution of the hydrogen atoms by deuterium, fluorine, or chlorine reduces the energy of the fundamental vibration, shifting the absorption out of the telecommunication window. For example, a fluorinated polymer waveguide can have losses below 0.2 dB/cm at 1.5 μm,[4] which is well acceptable for integrated optics devices with cm length scales.

Rare-earth ions are insoluble in a polymer film. This makes the fabrication of rare-earth doped polymer waveguides much more complicated than that of inorganic waveguides. In the latter case, the rare-earth ions can be incorporated rather easily using, e.g., ion implantation, melting, or deposition. As will be shown in this article, the doping problem in polymers can be solved using a variety of techniques. Section II of this article introduces an Er-doped organic polydentate cage complex, which encapsulates the rare-earth ion and makes it dissolvable into a polymer matrix. The optical properties of these complexes in solution are studied, and it is found that the emission bandwidth is very large. However, vibrational coupling to O—H and C—H bonds in the solvent/polymer partly quenches the optical transition.

In Sec. III, the optical properties of a lissamine-functionalized organic Nd complex doped into a polycarbonate waveguide are studied. Upon optical excitation, the highly absorbing lissamine becomes excited, whereupon Dexter energy transfer to the Nd^{3+} ion occurs. The effective absorption cross section of this process is four orders of magnitude higher than that for direct optical excitation of Nd. The lissamine sensitizer is not stable under illumination. This is discussed in more detail in Sec. III D, in which a model is proposed to describe the observed time dependence of the lissamine and Nd luminescence intensities. The highly absorbing sensitizer makes the standard butt–end coupling of the pump light into a waveguide amplifier impractical. For this reason, a waveguide configuration is introduced in Sec. IV, which gradually couples pump light from a pump waveguide into a parallel-placed signal guide. In this way, the pump power can be used more efficiently. The coupled mode theory for this design is described.

To solve the quenching problem of the rare-earth transition, a nanocomposite material is developed, that takes advantage of the good optical properties of silica as a host for the rare-earth ion, and the polymer as a waveguide material. In this composite, Er-doped silica colloids are embedded in a polymer waveguide. The SiO_2 colloids are fabricated using base-catalyzed wet chemical synthesis, and implanted with Er ions. Section V reports the properties of these Er-doped silica spheres. Very long luminescence lifetimes are found, which is partly attributed to the low local optical density of states in these colloids as described in Sec. VI. Finally, Sec. VII gives an outlook on optically and electrically pumped polymer waveguide amplifiers, discussing the most important materials requirements.

B. Optical experiments

Photoluminescence measurements were used throughout this study to optically characterize rare-earth doped materials. In most experiments, an Ar ion laser at various pump powers was used as the excitation source, as its emission overlaps with the absorption bands in the rare-earth ions. The laser beam was modulated at frequencies ranging from 10 to 40 Hz using a mechanical chopper or an acousto-optic modulator. The photoluminescence (PL) signal was focused into a monochromator and detected with a liquid N_2-cooled Ge detector or a photomultiplier tube, using standard lock-in techniques. The spectral resolution varied between 0.2–6 nm. In some cases, a 1.5 ns pulsed N_2 laser was used at a pulse energy of 20 μJ and a time resolution of $\sim$300 ps.

Luminescence lifetime measurements were performed by monitoring the decay signals after switching off the laser beam. The decay signals were averaged using a digitizing oscilloscope at a time resolution of 0.3 μs, or a photon counting system at a time resolution of 100 ns. All spectra were corrected for the detector response.

II. ERBIUM-DOPED ORGANIC POLYDENTATE CAGE COMPLEXES

A. Er-doped organic complexes

Inorganic Er salts cannot be dispersed directly into an organic matrix. To avoid this problem, the Er^{3+} ion is first encapsulated by an organic ligand. The resulting complex can then be dispersed in a polymer film. The ligand has to be designed such that it provides enough coordination sites to bind the Er^{3+} ion and to form a stable complex. Furthermore it may serve to shield the Er^{3+} ion from impurities in the surrounding matrix that may quench the luminescence. For

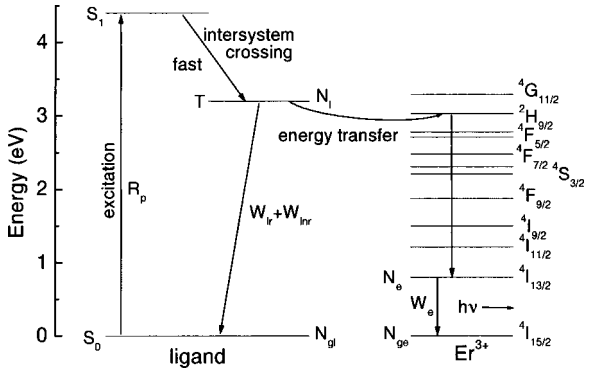

FIG. 1. Schematic diagram of the ligand-Er^{3+} system. The complex is first excited from the singlet S_0 ground state to the singlet S_1 state (exact position not known, but higher than 3.2 eV), followed by fast relaxation to the triplet T state. From there, energy transfer to the Er^{3+} $4f$ levels may take place. From these levels, rapid relaxation to the $^4I_{13/2}$ takes place. Finally the Er^{3+} may decay to the $^4I_{15/2}$ ground manifold by emission of a 1.54 μm photon.

example, O—H is known to quench the luminescence due to the coupling of the excited state of the ion to vibrational modes of the O—H bond.[5–7]

In this section, we study the optical properties of different Er-doped polydentate hemisperands, which form an overall neutral complex in which the Er^{3+} ion is encapsulated in a cage-like ligand configuration. Clear, room-temperature PL at 1.54 μm is observed for these complexes with a luminescence lifetime up to 0.8 μs. Selective deuteration experiments are carried out to study the possible quenching effect of C—H bonds. Exchanging C—H for C—D has shown to be beneficial for Eu^{3+}.[8]

Two different types of excitation are studied: direct excitation in one of the Er^{3+} manifolds using the 488 nm line of an Ar ion laser, and excitation via the organic ligand using the 337 nm line of a N_2 laser, followed by energy transfer to the Er^{3+} ion (see Fig. 1). The temperature quenching of the luminescence and the optical absorption cross sections are discussed, and finally a performance estimate for a planar optical amplifier based on these Er-doped complexes is made.

B. Sample preparation

Three different Er^{3+} complexes were prepared in a multistep synthesis, as discussed in detail in Ref. 8, and characterized by fast atom bombardment mass spectrometry, Fourier transform infrared spectroscopy, and elemental analysis. Figure 2(a) shows a schematic picture of a cyclic Er^{3+} complex in which the first coordination sphere consists of either C—H bonds (cyc-H), or C—D bonds (cyc-D). An acyclic Er^{3+} complex (acyc-H), sketched in Fig. 2(b), was also studied: it is open at the top and contains two $O(CH_2)_3CH_3$ groups. This is different than the cyclic complex which is closed at the top, with one $C_{18}H_{37}$ chain attached to the trivalent nitrogen atom. A three-dimensional representation of the cyclic complex is shown in Fig. 2(c).

After synthesis, the Er^{3+} complex solutions were dried, mixed with KBr and then pressed to 1 mm thick tablets with a diameter of 1.2 cm. The Er concentration is 1.0 wt. %. This

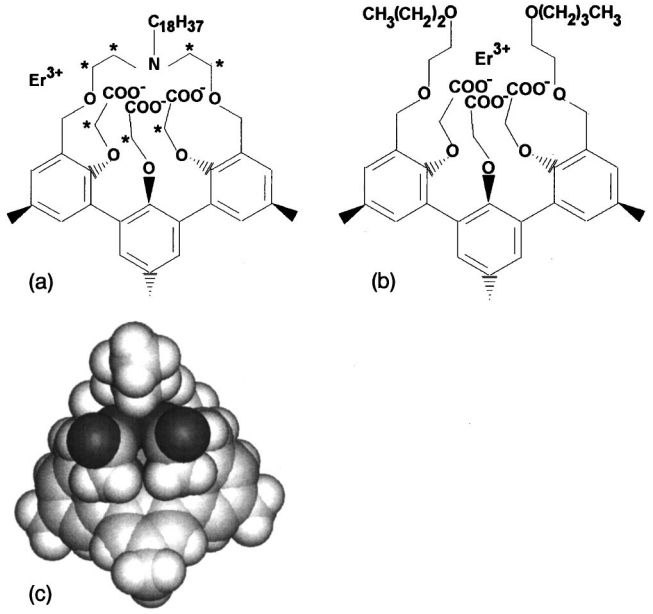

FIG. 2. Two-dimensional (2D) representation of the structure of (a) the cyclic Er^{3+} complex:* represents either 2 H (cyc-H) or 2 D (cyc-D) atoms, and (b) the acyclic Er^{3+} complex (acyc-H). The outer two benzene rings lie in one plane which is tilted backwards, whereas the middle benzene ring is tilted forwards. In this way, a cage is constructed, encapsulating the Er^{3+} ion. (c) Three-dimensional representation of the cyclic complex (cyc-H).

concentration does not take into account the (unknown) amount of water which may remain in the tablets as a result of the preparation process. To exclude the effect of quenching due to O—H in the host, some measurements were performed on solutions in deuterated butanol (>98%) at a complex concentration of 10^{-4} M or dimethylformamide (DMF) at a concentration of 2×10^{-3} M. In both solvents, acyc-H dissolved rather well, but the solutions with the cyclic complexes appeared somewhat turbid, indicating that not all the material had dissolved.

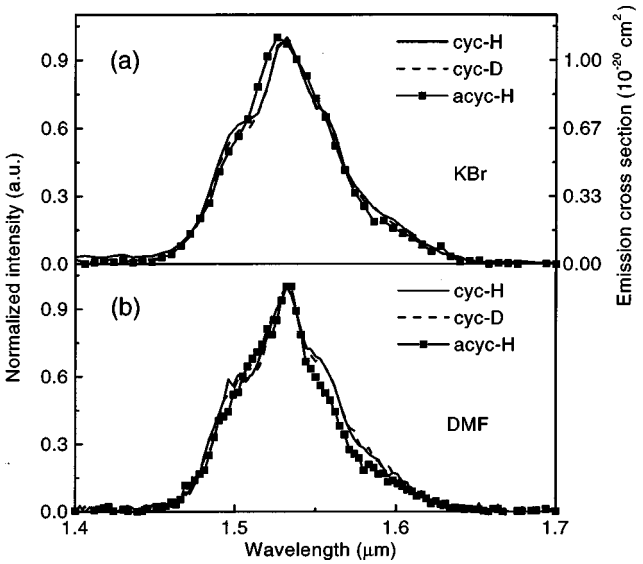

FIG. 3. Normalized room-temperature PL spectra of Er^{3+} complexes in (a) KBr tablets and (b) DMF, at a pump wavelength of 488 nm (power 100 mW).

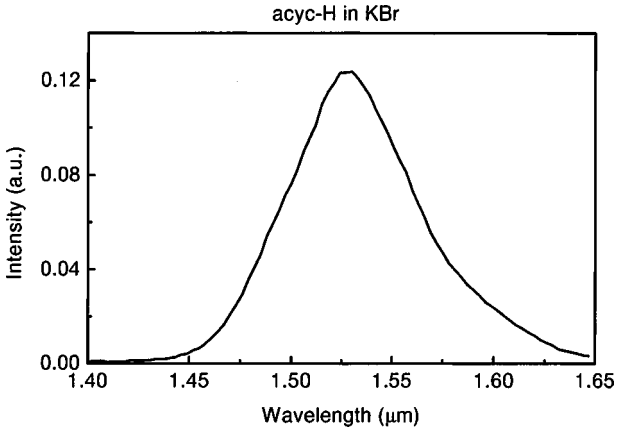

FIG. 4. Room-temperature spectrum of acyc-H in KBr after excitation via the ligand at 337 nm (pulse energy 20 μJ).

C. Optical characterization

Figure 3(a) shows normalized room-temperature PL spectra for the three complexes in KBr after excitation at 488 nm into the $^4F_{7/2}$ level (see Fig. 1). The peak around 1.54 μm is typical for Er^{3+} luminescence and is due to the transitions from the first excited state ($^4I_{13/2}$) to the ground state ($^4I_{15/2}$) manifolds. The full width at half maximum (FWHM) of all spectra is 70 nm. This is extremely wide for an Er-doped material: Er-implanted SiO_2 (11 nm FWHM),[9] phosphosilicate glass (25 nm FWHM),[10] sodalime silicate glass (19 nm FWHM),[11] Al_2O_3 (55 nm FWHM),[12] and fluorohafnate glass (64 nm FWHM).[13] Such a broad spectrum enables a wide gain bandwidth for optical amplification.

No comparison of the absolute PL intensities could be made for the three complexes, as the intensity varies over the KBr tablets (a factor of 2–3). The spectral shapes measured for the two cyclic complexes are identical, and slightly different from that for the acyclic complex. This difference is attributed to a small difference in local environment for the two types of complexes. Figure 3(b) shows the normalized room-temperature PL spectra for the Er^{3+} complexes in DMF solution. Again, the shape of the spectra observed for cyc-H and cyc-D are similar, but slightly different than that of acyc-H. Figure 4 shows the room-temperature PL spectrum of acyc-H in KBr after excitation at 337 nm (pulse energy 20 μJ). The 337 nm pump light is absorbed in the tail of the absorption band of the aromatic rings of the ligand. Energy transfer to the Er^{3+} ion then leads to excitation of the Er^{3+} resulting in the observed 1.54 μm luminescence.

Extinction spectra of the complexes in KBr were determined from reflection and transmission measurements as measured using a spectrometer and an integrating sphere (spectral resolution 0.3 nm), and are shown in Fig. 5. The absorption lines of the Er^{3+} ion are clearly visible and indicated in Fig. 5 (the level notation is given in Fig. 1). The steadily increasing background in the wavelength range down to 450 nm is attributed to scattering in the KBr tablets.

Using measured reflection data (not shown) and taking into account the known average areal density of Er in the samples (acyc-H: 8.54×10^{18} cm^{-2}, cyc-H: 8.21×10^{18} cm^{-2}, and cyc-D: 9.04×10^{18} cm^{-2}), the absorption

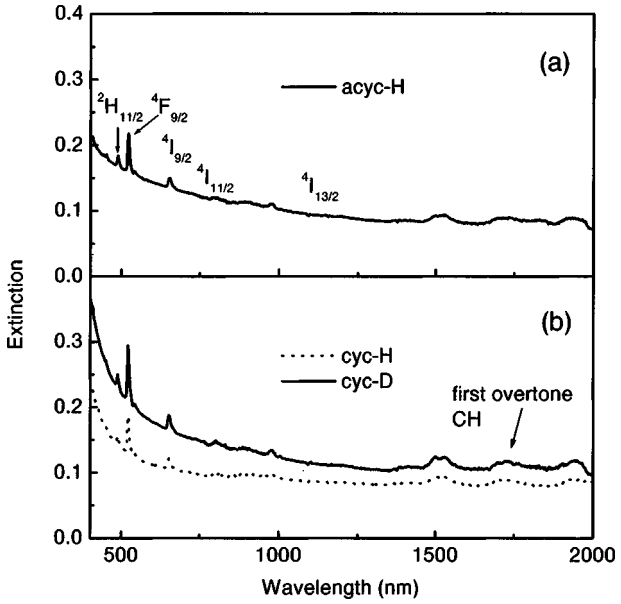

FIG. 5. Extinction spectra of the three Er^{3+} complexes in KBr, based on transmission measurements. (a) acyc-H, (b) cyc-H and cyc-D. The absorption peaks are indicated by the level notation of the absorption band.

cross sections at 1.5 μm for the $^4I_{15/2}\rightarrow{}^4F_{7/2}$ transition can be derived: $(0.62\pm0.05)\times10^{-20}$ cm^2 for acyc-H, $(1.1\pm0.4)\times10^{-20}$ cm^2 for cyc-H and $(0.93\pm0.05)\times10^{-20}$ cm^2 for cyc-D. These absorption cross sections are one to five times higher than the cross section at 1.5 μm of Er-doped glasses,[9,13] and for Er-implanted Al_2O_3.[14] This may be related to differences in average electron distribution around the Er^{3+} ion for organic complexes compared to inorganic hosts.

In practice, the peak absorption and emission cross sections for Er^{3+} are nearly the same. Under this assumption and using the cross section derived herein, the PL spectra of Fig. 3 can be converted to emission cross section spectra [see the right-hand side vertical scale of Fig. 3(a)]. From this spectrum, the radiative lifetime τ can be calculated:

$$\frac{1}{\tau}=\frac{8\pi n^2}{c^2}\int v^2\sigma_e(v)dv, \tag{1}$$

where n is the refractive index, c the speed of light, and v the optical frequency. Evaluating Eq. (1) yields a radiative lifetime of about 4 ms for these Er^{3+} complexes.

Luminescence decay measurements for cyc-H in KBr and the three Er^{3+} complexes in butanol-OD are shown in Fig. 6. Deconvolution of the decay curve of cyc-H in KBr results in a luminescence lifetime of 0.5 μs. In butanol-OD, the lifetimes for the three complexes are all around 0.8 μs. These lifetimes are much shorter than the radiative lifetime of 4 ms calculated from Eq. (1). This indicates that significant quenching of the Er^{3+} luminescence takes place.

Table I summarizes the total Er areal density and the PL intensity for the KBr tablets and DMF solutions. For all complexes, the areal density is typically a factor of 7 higher in KBr than in the DMF solutions, but the luminescence intensity is only a factor of 1.5–6 higher. This suggests that more luminescence quenching takes place in the KBr tablets than

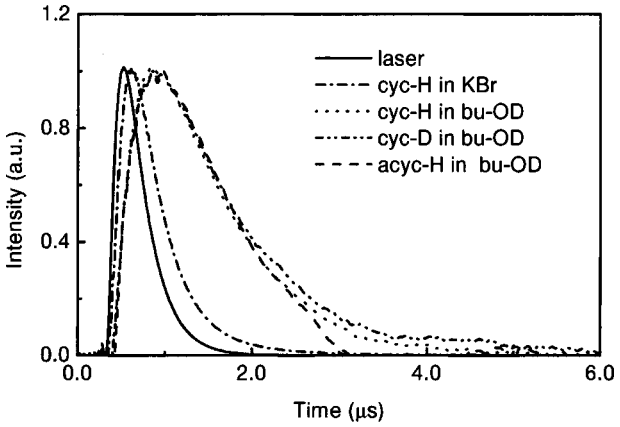

FIG. 6. Room-temperature decay measurements for the Er-doped organic complexes in KBr and butanol-OD, excited at 337 nm at a pulse energy of 20 μJ.

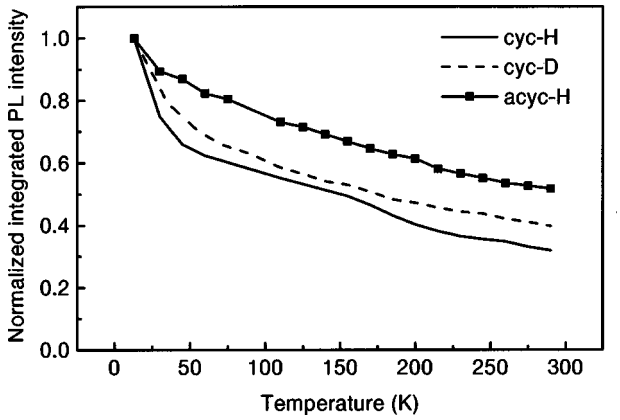

FIG. 7. Temperature dependence of the integrated 1.54 μm PL intensity of the Er^{3+} complexes in KBr (pump power 100 mW, excitation wavelength 488 nm).

in the DMF solutions. A possible explanation for this difference is a concentration quenching effect: due to the mixed crystalline nature of the tablets, local concentrations of Er^{3+} may be higher than the calculated average density. Due to the local high concentration, energy transfer from one Er^{3+} ion to another can occur and the excitation can migrate among these clustered regions, followed by quenching at a defect site in the tablet. As a result, the PL intensity will be lower and the luminescence lifetime shorter in the KBr tablets. In a solution where all the complexes are quite homogeneously dispersed, no concentration quenching will occur. This is confirmed by the longer luminescence lifetime for the complexes in butanol-OD solutions compared to the KBr tablets (see Fig. 6). However, even in solution the lifetimes are still much shorter than the expected 4 ms calculated from Eq. (1). There are three possible quenching mechanisms: (1) temperature quenching, (2) quenching by the nearest C—H neighbors, and (3) quenching by O—H groups.

1. Temperature quenching

Figure 7 shows measurements of the integrated 1.54 μm PL intensity between 15–300 K for the KBr tablets as measured using a closed-cycle He cryostat. Cyc-H and cyc-D show the same trend as a function of temperature, with a quenching by a factor 3 between 15 K and room temperature. For acyc-H, the temperature quenching is slightly smaller, a factor of 2 in the same temperature range. The quenching is small and can be mainly attributed to a decrease in the absorption coefficient as the temperature is increased (resulting in less efficient excitation). This indicates that temperature quenching, attributed to coupling to lattice vibrations, is not the major quenching mechanism.

2. Quenching by nearest C—H neighbors

The second order vibrational energy of C—H ($E_0 = 2960\ cm^{-1}$) is nearly resonant with the Er^{3+} first excited state ($E = 6500\ cm^{-1}$). This band around 1.7 μm can also be seen in Fig. 5. Thus, a C—H bond positioned near the Er^{3+} ion can quench the Er^{3+} luminescence. Such coupling should be less for C—D ($E_0 = 2100-2200\ cm^{-1}$). Comparison of the PL intensity of cyc-H with that of cyc-D for the DMF solutions (see Table I), shows that selective deuteration of the first coordination sphere has no influence on the PL intensity and thus it is concluded that quenching by these C—H bonds is not dominant.

3. Quenching by O—H groups

O—H groups are present in the liquids (mainly alcohols) used in the preparation of the Er^{3+} complexes, and they can also be present in the solvents used in the measurements: both DMF and butanol are highly hygroscopic. It is therefore very likely that O—H groups are coordinated to the Er^{3+} ion. Indeed, molecular dynamics simulations of rare-earth complexes in solution show that one O—H molecule can penetrate the first coordination shell of the ion.[8] In particular, water may preferentially solvate the Er^{3+} ion.[15] It is the most potent quencher of rare-earth luminescence, and has a significantly stronger interaction to the rare-earth than, for in-

TABLE I. Summary of the total Er areal density and the corresponding PL intensities for the Er^{3+} complexes in KBr and DMF.

	Er areal density (cm^2)	Relative PL intensity
acyc-H (KBr)	8.5×10^{18}	142–193
acyc-H (DMF)	1.3×10^{18}	113
cyc-H (KBr)	8.2×10^{18}	210–410
cyc-H (DMF)	1.2×10^{18}	66
cyc-D (KBr)	9.0×10^{18}	178–242
cyc-D (DMF)	1.2×10^{18}	66

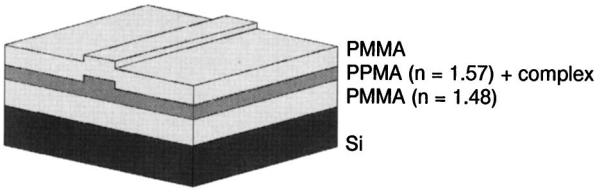

FIG. 8. Polymer channel waveguide structure for optical gain calculations. A high refractive index polymer ($n=1.57$, PPMA), doped with organic Er^{3+} complexes, is embedded in a low index polymer ($n=1.48$, PMMA) on top of a silicon substrate.

stance, alcohols. An O—H group positioned near the Er^{3+} ion will result in efficient quenching of the luminescence, because its first vibrational overtone ($E_0=3400\ cm^{-1}$) is strongly resonant with the $^4I_{13/2}\rightarrow{}^4I_{15/2}$ Er^{3+} transition ($E=6500\ cm^{-1}$). Work by Ermolaev *et al.*[16] shows that the rate constant for deactivation of the Er^{3+} excited state via O—H groups, located at a distance of 2.2–2.5 Å is in the order of $(3-5)\times10^8\ s^{-1}$, which is much larger than deactivation via C—D bonds at 2.2–2.5 Å ($k=5\times10^6\ s^{-1}$). This would explain that, with O—H attached to the complex, substitution of C—H by C—D will have no significant effect on the PL intensities measured in solution (see Table I).

D. Optical gain calculation

With the coefficients determined in the previous paragraphs, an estimate of the threshold pump power for a planar optical amplifier based on Er-doped organic complexes can be made. In such a polymer channel waveguide, a high refractive index polymer [e.g., poly(phenylmethacrylate) (PPMA), $n=1.57$] doped with organic Er complexes, is embedded in a low index polymer [e.g., poly(methylmethacrylate) (PMMA), $n=1.48$] (see Fig. 8). A typical waveguide core dimension is $2\times1\ \mu m^2$.

A calculation is done for direct excitation of Er^{3+} into the $^4F_{7/2}$ excited state (see Fig. 1). Assuming that the population of the $^4F_{7/2}$ state decays rapidly to the first-excited state, the rate equations reduce to those for a quasi two-level system.[17] Solving these rate equations for steady-state conditions, the populations become:

$$N_g=\frac{W_e}{W_e+R}N, \tag{2}$$

$$N_e=\frac{R}{W_e+R}N, \tag{3}$$

where $R=\sigma_aP\lambda/(hca)$ is the Er^{3+} excitation rate, N_e is the population of the first excited state, N_g is the population of the ground state, N is the Er^{3+} concentration, $W_e=1/\tau_e$ the erbium decay rate, P is the pump power in the waveguide, σ_a is the absorption cross section, $\lambda=488$ nm is the excitation wavelength, and a the waveguide core cross section. As a first estimate, we have taken the (unknown) absorption cross section at 488 nm equal to the measured value at 1.53 μm from Sec. II C. The differential optical gain (dB/cm) is given by $10\times^{10}\log(I/I_0)$, where I_0 is the intensity at the beginning of the waveguide and $I=I_0e^{kx}$ is along the waveguide, with k as the gain factor given by:

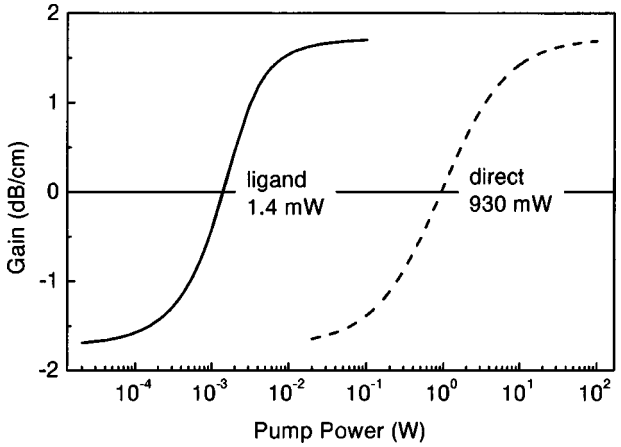

FIG. 9. Calculated differential optical gain as a function of pump power for direct excitation (dashed line) and for excitation via the ligand (solid line) for a waveguide amplifier with a $2\times1\ \mu m^2$ cross section. The threshold power is indicated for each calculation.

$$k=\sigma_e(N_e-N_{ge})\alpha, \tag{4}$$

with α as the estimated fraction of light which is confined in the core of the waveguide, and σ_e as the emission cross section from Sec. II C. The optical gain as a function of pump power is calculated using the values given in Table II. The result is shown in Fig. 9. The maximum differential gain is 1.7 dB/cm, indicating that for instance a loss free (1×2) splitter could be made with a few cm long waveguide. The threshold pump power is 930 mW. This is much higher than the minimum power needed in Er-doped glass or Al_2O_3 amplifiers[18] and is due to the much smaller luminescence quantum efficiency of the Er^{3+} ion in the organic complexes as compared to that in the inorganic materials.

The power of 930 mW needed for optical amplification is relatively high. To reduce it, excitation of the complex via the aromatic part of the ligand, at 287 nm may be employed. At this wavelength, the absorption cross section of the ligand is about $8.5\times10^{-18}\ cm^2$, much higher than the cross section for direct absorption of the Er^{3+} ion at 488 nm. This makes excitation via the ligand very efficient. Energy transfer from the ligand excited state to the Er^{3+} ion then results in population of the Er^{3+} $^4I_{13/2}$ luminescent excited state. Taking this process into account, a gain calculation can be made. Assuming that the transition from the singlet (S_1) to the triplet (T) state of the ligand is fast (see Fig. 1), a quasi two-level system can be used for the ligand and the Er^{3+} ion. The rate equations then become:

$$\frac{dN_1}{dt}=R_1N_{gl}-W_{lr}N_1-W_{lnr}N_1N_{ge}, \tag{5}$$

$$\frac{dN_e}{dt}=-W_eN_e+W_{lnr}N_1N_{ge}, \tag{6}$$

in which $R_1=\sigma_1P\lambda/(hca)$ is the ligand excitation rate, N_e and N_1 are the population fraction of the first-excited state of Er^{3+} ion and the ligand, respectively, N_g and N_{gl} are the population fraction in the ground state of Er^{3+} ion and the ligand, respectively, W_{lr} is the ligand radiative decay rate, W_{lnr} is the ligand nonradiative decay rate (transfer rate), and

TABLE II. Typical values for the parameters used in the optical gain calculation of an Er-doped planar polymer optical amplifier using direct or indirect optical pumping.

Parameter	Symbol	Value
Erbium decay rate	W_e	1.25×10^{6} s^{-1}
Erbium absorption cross section $\lambda=488$ nm	σ_a	1.1×10^{-20} cm^2
Erbium emission cross section $\lambda=1.54$ μm	σ_e	1.1×10^{-20} cm^2
Waveguide cross section	a	2×1 μm^2
Total erbium concentration	N	9×10^{19} cm^{-3}
Estimated fraction of light confined in the core	α	0.4
Ligand absorption cross section	σ_1	8.5×10^{-18} cm^2
Ligand radiative decay rate	W_{lr}	2×10^{8} s^{-1}
Ligand nonradiative decay rate	W_{lnr}	1×10^{9} s^{-1}

σ_1 is the ligand absorption cross section. Solving these equations for steady-state conditions, the differential gain can be calculated using Eq. (4) and typical values given in Table II. The result is also plotted in Fig. 9. The threshold pump power reduces from 930 to 1.4 mW. These low pump powers are very interesting for practical applications. Note that in the final design pump loss has to be taken into account, as will be discussed in Sec. IV. The next challenge is to engineer the ligand and to shift the excitation wavelength to the visible in order to be able to use standard semiconductor lasers as pump lasers. Alternatively, sensitizers with a high absorption coefficient and a high intersystem crossing efficiency may be attached to the complex, to further optimize the pump efficiency. This is described in Sec. III. Finally, we note that the aforementioned calculations do not take into account upconversion effects, which may increase the pump power needed for amplification.[19] More measurements are required to determine the cooperative upconversion and excited state absorption cross sections for these Er-doped organic complexes.

III. LISSAMINE FUNCTIONALIZED Nd^{3+} COMPLEXES IN POLYMER WAVEGUIDES AND SOLUTION

A. Sensitized Nd^{3+} complexes

In Sec. II, we have shown that optically active Er-doped polydentate cage complexes can be synthesized, and they emit room-temperature luminescence at 1.535 μm when optically excited either directly into an Er intra-4f level, or indirectly via the cage which also acts as a chromophore.[20] We found that the luminescence lifetime of these complexes is rather short (0.8 μs), which was attributed to energy transfer of the excited state of the Er^{3+} ion to O—H vibrational states of the solvent molecules.[16,21]

Obviously, these nonradiative quenching processes are a disadvantage of the use of organic cage complexes. On the other hand, an advantage is that highly absorbing antenna chromophores can be incorporated in the organic complex. Once this chromophore is excited it can transfer its excitation energy to the rare-earth ion by a Dexter mechanism. If the energy transfer from chromophore to rare-earth ion is efficient, this process strongly enhances the excitation efficiency of the rare-earth ion.

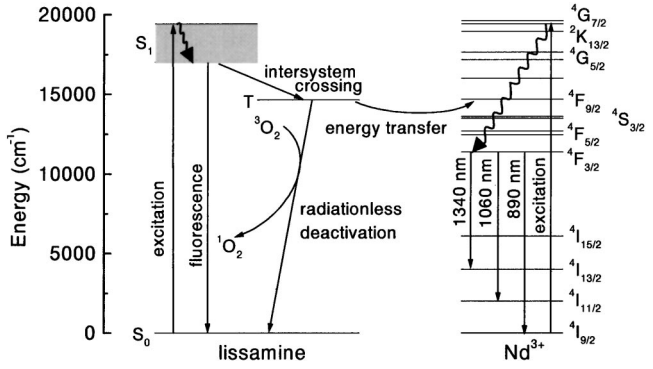

FIG. 10. Schematic energy level diagram of the lissamine Nd^{3+} complex. The arrows indicate the excitation mechanisms of the Nd^{3+} ion: either directly into the $^4G_{7/2}$ level by pumping at 515 nm, or through the lissamine sensitizer ($S_0\rightarrow S_1$ transition followed by intersystem crossing and energy transfer).

In this section, we will report the optical properties of terphenyl-based Nd^{3+} complexes with and without a highly absorbing lissamine antenna chromophore. The neodymium (Nd) ion has an intra-4f transition from the $^4F_{3/2}$ to the $^4I_{11/2}$ level at 1.34 μm, which coincides with the low dispersion window of standard silica optical fibers. Complexes were dissolved either in hexadeuterodimethylsulfoxide (DMSO-d6) solutions or in partially fluorinated polycarbonate planar waveguides. In complexes without lissamine, excitation of the Nd^{3+} ion at a wavelength of 515 nm leads to population of the $^4G_{7/2}$ level, from where it decays to the $^4F_{3/2}$ level (see Fig. 10). Decay from this level leads to the characteristic Nd^{3+} luminescence at 890, 1060, and 1340 nm due to transitions to the $^4I_{9/2}$, $^4I_{11/2}$, and $^4I_{13/2}$ levels, respectively. In complexes with the lissamine sensitizer, the 515 nm light is mainly absorbed by the highly absorbing lissamine, which becomes excited into the singlet state (S_1). This is followed by intersystem crossing to the triplet state (T, $E_T=14\,600$ cm^{-1}) (see Fig. 10). From the triplet state energy transfer to the Nd^{3+} ion can occur, which results in excitation of the Nd^{3+} ion into the $^4S_{3/2}$ and $^4F_{9/2}$ levels. After relaxation to the $^4F_{3/2}$ level, the 890, 1060, and 1340 nm luminescence can be observed.

B. Sample preparation

Terphenyl-based Nd^{3+} complexes were synthesised using the procedure described in Ref. 22. Some complexes were functionalized with lissamine, a Rhodamine-B derivative.[23] Figure 11 shows a schematic picture of the structure of the terphenyl-based Nd^{3+} complexes [Fig. 11(a)] with two benzoyl side-groups (Bz.Nd) and [Fig. 11(b)] with one benzoyl side-group and a lissamine sensitizer (Ls.Nd). Both complexes have a cage-like configuration, encapsulating the Nd^{3+} ion. The complexes were dissolved in DMSO-d6 to a concentration of 10^{-2} M for Bz.Nd and 10^{-6} M for Ls.Nd, or dissolved in partially fluorinated polycarbonate[24] waveguides at a concentration of 1, 3, and 10 wt.% (complex). The polycarbonate waveguides were made by spin coating a cyclohexylacetate solution of polycarbonate and complex onto a Si substrate covered with a 3

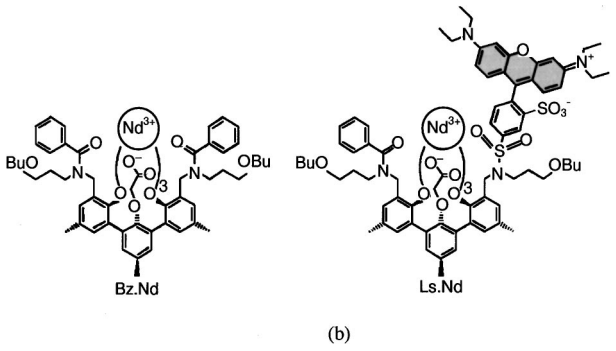

FIG. 11. Schematic picture of (a) benzoyl-Nd^{3+} complex (Bz.Nd) and (b) lissamine functionalized Nd^{3+} complex (Ls.Nd).

μm thick thermally grown SiO_2 layer or a microscope glass slide. The spin coating was performed for 30 s at a spinrate of 3000 rpm and followed by thermal annealing at 190 °C (in a vacuum) for 1 h. The thickness of the polymer layer was 3.55 μm.

The light intensity transmitted through the film on the microscope glass slide was monitored using a silicon photodiode positioned behind the sample, and changes in transmission were converted to absorption coefficients using the known film thickness and Lambert–Beer's law. Absorption spectra were measured before and after laser illumination using a variable-angle spectroscopic ellipsometer.

C. Luminescence properties

Figure 12 shows the PL intensities at 1060 nm for a 10^{-2} M solution of Bz.Nd and a 10^{-6} M solution of Ls.Nd (lissamine sensitized), both in DMSO-d6, at different excitation wavelengths as available from the Ar ion laser. The pump power for excitation was 60 mW for all excitation wavelengths. The absorption spectrum measured for the same solutions, measured using a spectrophotometer, is also included in Fig. 12 (drawn lines). The excitation spectrum for the complex without sensitizer (Bz.Nd) shows some structure, which is roughly similar to that found in the absorption measurement, and is consistent with the absorption bands of the Nd^{3+} ion around 475 and 513 nm. The excitation spectrum for the complex with sensitizer (Ls.Nd) shows a completely different behavior: the 1060 nm emission intensity increases strongly with excitation wavelength, again very similar to what is found for the absorption spectrum. Given the fact that the lissamine complex shows a broad absorption band around 580 nm, this clearly indicates that the excitation of Nd^{3+} around 500 nm takes place via the sensitizer. The absorption of the lissamine occurs at the xanthene unit [i.e., the gray part in the structure for Ls.Nd in Fig. 11(b)]. Note that the measured absorption cross section is in the 10^{-17} cm^2 range, four orders of magnitude higher than the typical Nd^{3+} intra-4f transition cross section.

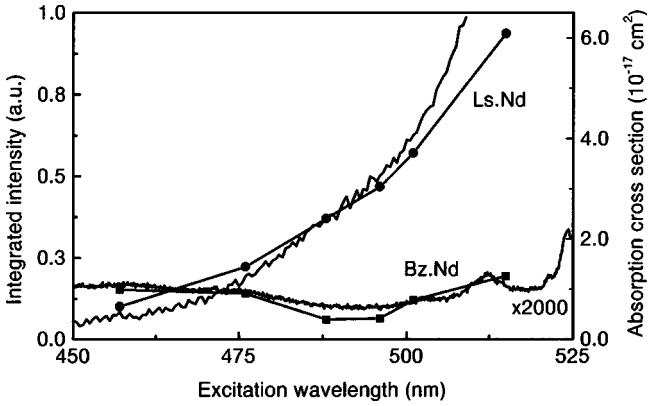

FIG. 12. PL at 1060 nm as a function of excitation wavelength for the benzoyl-Nd^{3+} complex (Bz.Nd) (10^{-2} M, squares) and the lissamine functionalized Nd^{3+} complex (Ls.Nd) (10^{-6} M, circles) in DMSO-d6 solutions. The absorption spectra of Bz.Nd and Ls.Nd are also shown (drawn lines). Note that the absorption data for the Bz.Nd solution are multiplied by a factor of 2000.

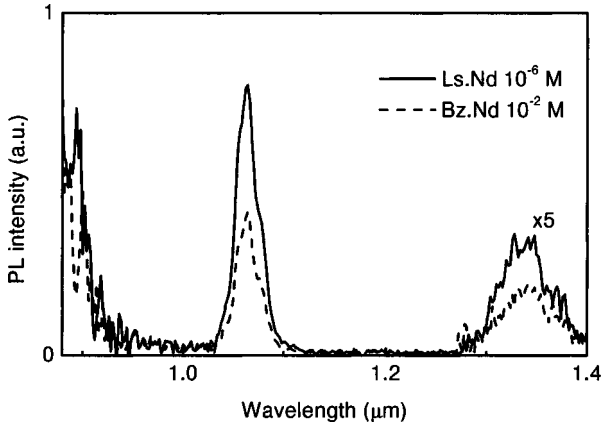

FIG. 13. PL spectra of the lissamine functionalized Nd^{3+} complex (Ls.Nd) (10^{-6} M) and the benzoyl-Nd^{3+} complex (Bz.Nd) (10^{-2} M) in DMSO-d6 solutions. The excitation wavelength is 515 nm, at a pump power of 60 mW. Note that around 1340 nm, the spectra are multiplied by a factor of 5.

Figure 13 shows room-temperature PL spectra for 10^{-2} M Bz.Nd and 10^{-6} M Ls.Nd in DMSO-d6, recorded using excitation at 515 nm at a pump power of 60 mW. The complexes show room-temperature PL of Nd^{3+} at 890, 1060, and 1340 nm. Although the concentration of Ls.Nd is 10^4 times lower than the concentration of Bz.Nd, the PL intensity is two times higher. Optical absorption measurements at 515 nm for both solutions show an almost equal absorption: 0.033 cm^{-1} for 10^{-2} M Bz.Nd and 0.031 cm^{-1} for 10^{-6} M Ls.Nd. The fact that the sensitized complex shows a higher luminescence intensity than the complex without a sensitizer, even though the measured absorption was the same, indicates that the internal energy transfer efficiency within the sensitized complex is quite high. The factor of 2 difference can be due to the fact that upon direct excitation into the higher lying state of the Nd^{3+} ion, the Nd^{3+} ion can also decay radiatively to the ground level (indeed, 524 nm luminescence has been observed, resulting from the transition from the $^2K_{13/2} \rightarrow {}^4I_{9/2}$ transition), leading to a lower quantum yield for the near-infrared transitions in the case of direct optical excitation of the Nd^{3+} at 515 nm.

The measured luminescence lifetime at 1060 nm for the Bz.Nd complex in DMSO-d6 is 2.5 μs (not shown), and for the sensitized Ls.Nd complex 2.2 μs. The luminescence lifetime of Nd^{3+} in inorganic materials can be as high as 250 μs.[25] The low quantum yield in the organic complexes is

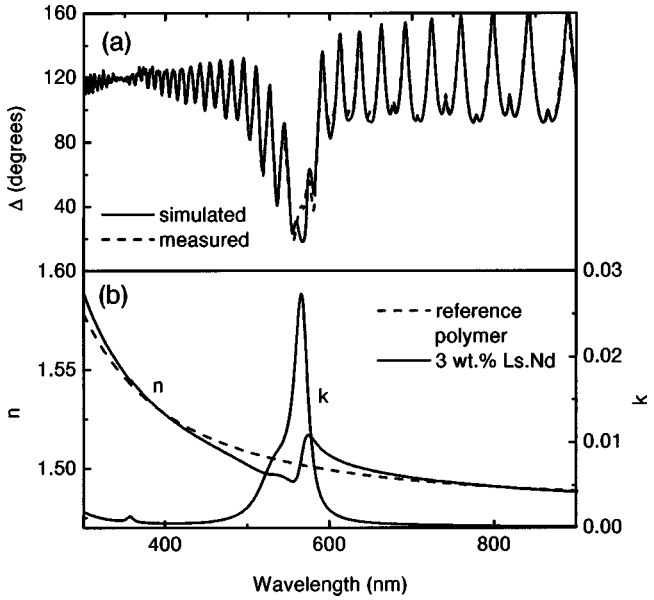

FIG. 14. (a) Measured and calculated ellipsometric parameter Δ as a function of wavelength for a partially fluorinated polycarbonate waveguide doped with 3 wt. % lissamine functionalized Nd^{3+} complex (Ls.Nd). (b) Real (n) and imaginary (k) part of the refractive index derived from the simulation data indicated by the solid line in (a). The real index for an undoped reference waveguide is shown for reference [dashed line in (b)].

attributed to quenching of the Nd^{3+} excited state by coupling to overtones of nearby C—H and O—H vibrational states.

Figure 14(a) shows the measured (dashed line) and simulated (solid line) ellipsometry parameter Δ as a function of wavelength for a partially fluorinated polycarbonate planar polymer waveguide doped with 3 wt. % Ls.Nd. The measurements were done using a variable-angle spectroscopic ellipsometer. The interference structure is caused by reflections at the air/polymer, polymer/SiO_2, and SiO_2/Si interfaces. A clear dip in Δ is observed around 580 nm, which is caused by the high absorption of the lissamine. The simulated data are based on a Lorentz oscillator model and correspond well with the measured data. From the simulation parameters, the real (n) and imaginary (k) part of the refractive index of the Nd-doped polymer waveguide layer can be calculated, as shown in Fig. 14(b). Also shown is the measured refractive index of an undoped reference polymer. Outside the resonance region, the refractive index of the Nd-doped waveguide layer is very similar to that of the undoped layer, indicating that the spincoating technique leads to Nd-doped waveguide layers with similar density as pure waveguide layers. The maximum value of k is 0.027 at 580 nm which corresponds to an absorption cross section of 4.5×10^{-16} cm^2, which is roughly two to three times higher than the literature value for Rhodamine-B.[14] It is clearly seen that the high absorption of the lissamine causes a change in the real part of the refractive index around 580 nm as described by Kramers–Kronig theory.

Optical losses were measured using the sliding prism method.[26] Diiodomethane was used as an index matching liquid for optimum output coupling. A white light source as well as lasers operating at 633, 838, 1305, and 1565 nm were used. Measurements were performed on an undoped partially fluorinated polycarbonate waveguide. The result is shown in Fig. 15. The peak around 1650 nm is due to overtone absorption by C—H bonds. The band around 1400 nm is attributed to absorption by C—H bonds and O—H bonds in the polymer. The two peaks around 1150 nm arise from second overtone absorption by aromatic and aliphatic C—H bonds. The background loss at the Nd^{3+} emission wavelengths is <0.05 dB/cm at 1060 nm and 0.08 dB/cm at 1305 nm. This indicates that these polycarbonate waveguides are ideally suited for planar waveguide applications.

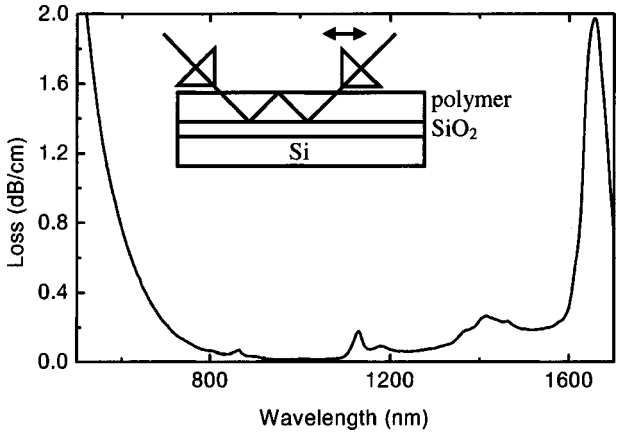

FIG. 15. Optical loss spectrum of an undoped partially fluorinated polycarbonate waveguide measured using the sliding prism method (see inset).

Figure 16 shows the PL spectra of a 3 wt. % Ls.Nd-doped fluorinated polycarbonate waveguide excited at a wavelength of 515 nm. The dashed line shows the luminescence measured using excitation and collection of the light from the top of the sample ($P=40$ mW). The 890 and 1060 nm luminescence of the Nd^{3+} ion are clearly seen. Spectra taken in the near-infrared region (not shown) also show the 1340 nm luminescence. The emission observed in the lower wavelength region is due to luminescence of the lissamine, which has a peak emission wavelength ($S_1 \rightarrow S_0$ transition) at

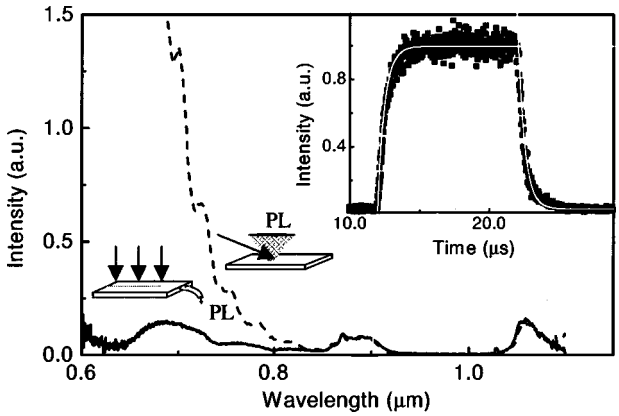

FIG. 16. PL spectra of a polymer waveguide doped with 3 wt. % lissamine functionalized Nd^{3+} complex (Ls.Nd). The dashed line indicates the spectrum collected from the top of the waveguide using excitation at 515 nm at a power of 40 mW. The solid line indicates the spectrum using excitation at 515 nm at a power of 140 mW and collected from the output facet of the waveguide using a multimode optical fiber. Schematics of the two measurement configurations are shown. The inset shows the time dependence of the 1060 nm luminescence upon pulsed excitation.

580 nm. The small peaks at the shoulder of the lissamine luminescence are attributed to an interference effect in the waveguide layers. The solid line in Fig. 16 is the spectrum observed for excitation from the top ($P=140$ mW and spot 5×15 mm^2) and collecting from the output facet of the waveguide using a multimode fiber. Again, the 890 and 1060 nm luminescence are observed, but here the luminescence of the lissamine is strongly decreased, which is attributed to the reabsorption by the lissamine itself. This indicates that self-absorption should be taken into account when designing waveguide devices.

The inset of Fig. 16 shows the time dependence of the 1060 nm PL signal after switching the 515 nm pump on and off. An exponential fit through the decay part results in a PL lifetime of 0.8 μs. This is significantly lower than the decay measured for complexes in DMSO-d6 solution (2.2 μs), which indicates that quenching by C—H and O—H groups in the polymer matrix also contributes to the radiation-less deactivation of the Nd^{3+}.

The energy transfer from the lissamine to the Nd^{3+} ion occurs via the triplet state of the lissamine. However, the triplet state can also be quenched by, e.g., O_2 that is always present in solution or in a polymer film.[27,28] In order to investigate this, we measured the Nd^{3+} luminescence intensity of Ls.Nd in DMSO-d6 solutions before and after degassing (not shown). The Nd^{3+} PL intensities were similar, indicating that quenching by O_2 does not play a role in the DMSO-d6 solutions. As it is known that the quenching rate by O_2 in solution is about 10^7 s^{-1}, it can be estimated that the intramolecular energy transfer rate to the Nd^{3+} ion has to be $>10^7$ s^{-1}.[29] This transfer rate is of the same order of magnitude as for triphenylene sensitized Eu^{3+} in acetonitrile solutions.[30]

A space filling model of Ls.Nd, in which all atoms are represented by their van der Waals radius, shows that the distance between lissamine and the Nd^{3+} ion is 7–8 Å, whereas the effective average Bohr radius for the excited lissamine and the unexcited Nd^{3+} ion is about 2.5 Å. According to Dexter,[31] this means that 3% of the maximum possible energy transfer rate is reached. This could be improved by reducing the distance between the lissamine and the Nd^{3+} ion by changing the configuration of attachment of the lissamine. Another possibility to increase the energy transfer rate is to improve the spectral overlap between the sensitiser and the Nd^{3+} energy levels.[32] In the present case, the energy of the triplet state of lissamine matches with the 14 600 cm^{-1} band of Nd^{3+} which shows weak absorption. If a sensitizer could be used that matches the strong $^4I_{9/2}\rightarrow{}^4S_{3/2}$ absorption band (13 600 cm^{-1}), the energy transfer rate could be increased.

D. Photodegradation of lissamine-functionalized Nd^{3+} complexes

Figure 17(a) shows time-dependent measurements of the 580 nm lissamine luminescence during illumination performed on polymer waveguides doped with 3 wt. % (complex) for near-normal incidence irradiation at three different pump powers. Each measurement was made on a fresh spot at the sample. The luminescence signal was detected normal to the waveguide. For a pump power of 4 mW the luminescence intensity slowly rises to a maximum and then decreases again. At higher pump powers, the same effect is observed, but both the increase and the decrease processes occur faster. This photodegradation process may be the result of oxygen induced quenching. Another possibility is that upon photoexcitation radicals are formed, which react with the sensitizer.[33] Figure 17(b) compares the luminescence intensity versus illumination time for 1 and 3 wt. % films. The 1 wt. % doped film does not show the initial increase in the luminescence intensity. This might indicate that concentration quenching plays a role in the time-dependent behavior as well.

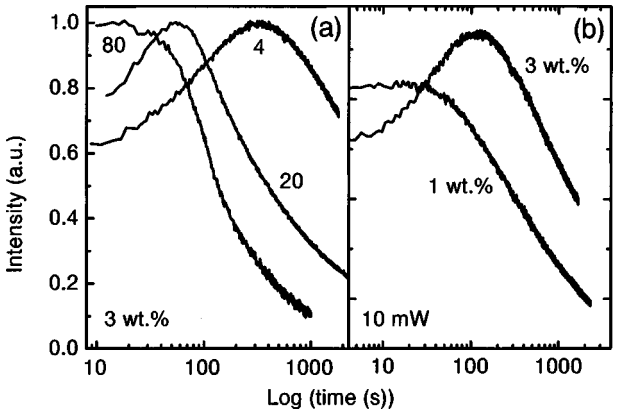

FIG. 17. (a) 580 nm lissamine PL of a polymer waveguide doped with 3 wt. % lissamine functionalized Nd^{3+} complex (Ls.Nd) at pump powers of 4, 20, and 80 mW. Each measurement was made at a fresh spot on the sample. (b) Similar measurements on a 3 and 1 wt. % Ls.Nd-doped waveguide at a pump power of 10 mW.

Figure 18(a) shows the luminescence spectra of a lissa-

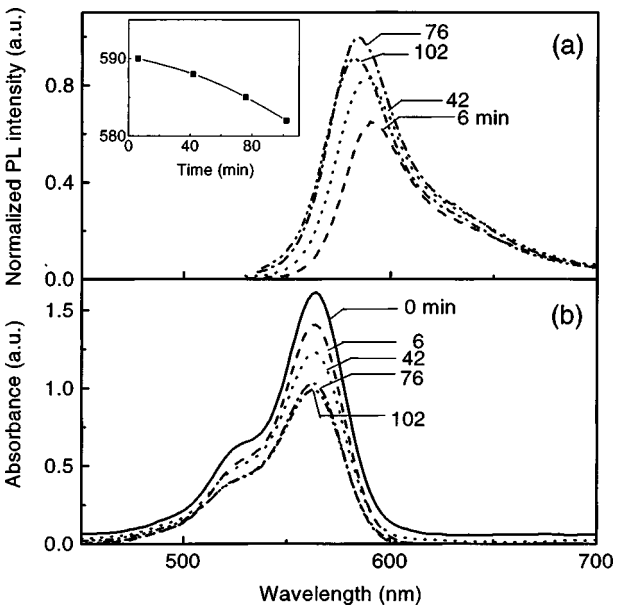

FIG. 18. Luminescence (a) and absorption (b) spectra of the lissamine sensitizer for different illumination times. The excitation wavelength was 488 nm at a pump power of 1 W in a 5 mm spot. The inset shows the peak position in nm as a function of the illumination time.

mine Nd complex-doped polymer film excited at an excitation wavelength of 488 nm at a pump power of 1 W and a spot diameter of 5 mm. The emission is attributed to fluorescence from the lissamine sensitizer. The time to take each spectrum was 6 min, and the time given in Fig. 18 is the total elapsed time at the end of the measurement. As can be seen from the spectra, continued illumination results in a small blueshift of the peak luminescence from the lissamine sensitizer, as is also shown in the inset of Fig. 18. The integrated luminescence intensity increases for the first three measurements, and then decreases. The absorption spectra of the lissamine/Nd complex-doped polymer film for different illumination times are shown in Fig. 18(b). As can be seen, the spectral shape of the absorption spectrum remains the same, but the absorption decreases upon illumination. The blueshift and the increase in the intensity of the luminescence spectra could, in principle, be explained by the bleaching of dimers or aggregates of complexes, that may be present at the high concentrations applied,[34–36] because these species have a different emission spectrum than monomers due to the electronic interaction between the molecules. However, this should also result in a change of the shape of the absorption spectrum upon bleaching, which is not observed in Fig. 18(b), so that this dimer bleaching model may be excluded. Alternatively, the blueshift can be explained by a change in self-absorption as the density of optically active lissamine decreases upon illumination [as seen in Fig. 18(b)]. Figure 18 shows that the absorption and emission spectra of lissamine strongly overlap. The absorption cross section of lissamine, determined in Sec. III, is 4.5×10^{-16} cm^2 at 580 nm and the concentration in the 1 μm thick film is 5×10^{19} cm^{-3}, which results in an absorption depth of roughly 0.5 μm. This means that a rather large fraction of the lissamine luminescence is reabsorbed by the surrounding lissamine molecules. As the concentration of optically active lissamine is reduced due to the illumination, the self-absorption reduces, and as a result, the collected luminescence intensity can increase in the region where the absorption and emission spectra overlap. This results in an apparent blueshift of the luminescence spectrum, as is observed in Fig. 18(a).[37] Note that the pump absorption depth at 488 nm is 6.6 μm, so that absorption by the lissamine causes no significant depletion of the pump intensity through the film.

Figure 19 shows measurements of the lissamine luminescence at 580 nm as well as the Nd^{3+} luminescence at 880 nm as a function of illumination time. The pump power was 1 W at an excitation wavelength of 515 nm, and a spot diameter of 1 mm. The Nd^{3+} emission spectrum does not show a spectral change upon illumination (not shown). The lissamine luminescence first increases and then decreases as was also seen in Fig. 18(a). Also shown is the absorption coefficient measured at 515 nm during illumination (crosses), which shows that the concentration of optically active lissamine is gradually decreasing. Without self-absorption, the lissamine luminescence intensity would scale with the absorption coefficient, but at high lissamine concentration (short illumination time), the self-absorption reduces the detected luminescence intensity. This would result in a more constant intensity for short times, but it cannot explain

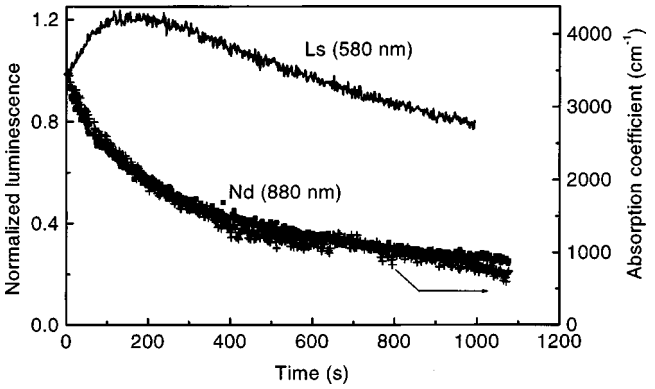

FIG. 19. Lissamine luminescence intensity (580 nm, solid line) and Nd^{3+} luminescence intensity (880 nm, solid squares) as a function of illumination time. Also shown is the absorption coefficient of the film measured at 515 nm during illumination (crosses). A pump excitation wavelength of 515 nm at a power of 1 W and a 1 mm diameter spot was used.

the initial increase in the luminescence intensity as observed in Fig. 19. The increase may be explained by a concentration quenching model: at the high lissamine concentration used (10 wt. %), the lissamine molecules are spaced by only a few nm, so that excitations can easily transfer from one lissamine to another by a Förster energy transfer mechanism. In this way, the excitation can migrate through the film, until it reaches a quenching center and is lost. In such a quenching model, the luminescence quantum efficiency increases with decreasing lissamine concentration. So, if the active lissamine concentration reduces as a result of illumination, the quantum efficiency increases. This additional reduction of the luminescence intensity for high concentration can describe the initial increase in the luminescence intensity with time. For a lower intrinsic lissamine concentration in the film, one would expect the initial increase to be smaller or even absent. Indeed, this is seen in Fig. 17(b) for a 1 wt. % doped polymer film. Using the combined effect of self-absorption and concentration quenching, the data of Fig. 19 can be described qualitatively. A quantitative description could not be made, which is ascribed to several unknown effects such as changes in the refractive index as a result of the photobleaching, changes in the active lissamine depth profile within the layer due to the gradient of the pump power in the film, and the effect of the standing wave pattern in the pump intensity throughout the film, which results from multiple reflections at the interfaces of the layers.

As can be seen in Fig. 19, the Nd^{3+} luminescence intensity shows a completely different time dependence than the lissamine luminescence: it precisely follows the decrease in absorption coefficient due to the decreasing active lissamine concentration. As the excitation of the Nd^{3+} ion occurs via the triplet state of the lissamine, one would also expect an initial increase in the Nd^{3+} luminescence. However, this is not observed. One way to explain the different behavior of the lissamine and Nd intensities is by assuming that two types of complexes exist in the polymer film. One which shows the behavior as observed in Fig. 19, explained by concentration quenching, and that does not couple to the Nd^{3+} ion (denoted as Ls), and one that couples to the Nd^{3+}

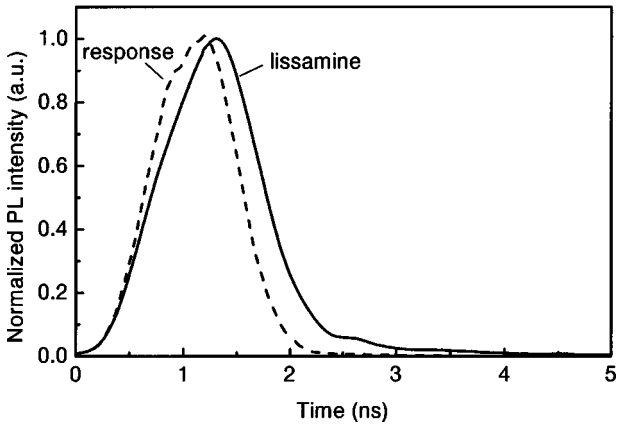

FIG. 20. Time-dependent luminescence trace at $\lambda = 580$ nm for a lissamine/neodymium doped polymer film (solid line) after excitation with a 1.5 ns (FWHM) pulse at 337 nm and a pulse energy of 20 μJ. The dashed line shows the system response after excitation.

ion, but does not show concentration quenching (denoted as Ls.Nd). The fact that no concentration quenching would be observed for complexes that couple to Nd^{3+} could be explained by the ''heavy-atom'' effect.[38,39] The presence of a heavy atom like Nd increases the intersystem crossing rate within the lissamine.[22,40] If the intersystem crossing rate would be larger than the effective quenching rate due to concentration quenching ($\sim 10^8$ s^{-1}, in the order of the luminescence decay rate) the latter would not be observed.

To study the heavy atom effect, we have performed measurements of the luminescence lifetime of the lissamine singlet state at 580 nm on Ls and Ls.Nd complexes in dimethylsulfoxide (not shown), and found a luminescence lifetime of 2.6 ns for the free lissamine and 1.2 ns for the complex. Assuming that this reduction in luminescence lifetime is the result of an increase in the intersystem crossing rate due to the presence of Nd^{3+}, the intersystem crossing rate in the presence of the Nd^{3+} ion can be calculated to be 4×10^8 s^{-1}. Indeed, this is much higher than the intrinsic intersystem crossing rate of pure lissamine, which is known to be 8×10^6 s^{-1}. Note that these measurements were done in solution, in which the equilibrium position of the sensitizer with respect to the Nd^{3+} ion can be substantially different compared to that in a polymer film, and hence the found intersystem crossing rate may not be representative for the polymer film. However, these data clearly indicate the possible effect of Nd on the intersystem crossing rate and hence, as argued herein, on the concentration quenching. Streak images of the lissamine luminescence of a lissamine complex-doped film were measured after excitation at 337 nm using a 1.5 ns-pulsed N_2 laser. The streak image displays the luminescence intensity versus time and wavelength. Figure 20 shows time-dependent measurements of the 580 nm emission of a lissamine-doped film, together with the system response. A streak image is normally built up by luminescence spectra of different species in the sample, having different luminescence lifetimes. Singular value decomposition (SVD)[41] can be performed on the two-dimensional streak data set in order to derive the number of individual components that contribute to the streak image. Using SVD on the lissamine streak image, two contributions were found, one with a time component in the order of the system response (300 ps) and one with a time component of $\sim$0.6 ns. The luminescence spectra corresponding to the two time components were identical to the lissamine luminescence spectrum, which is consistent with the aforementioned assumption of the existence of two different types of lissamine complexes. In that case, the lissamine complexes exhibiting energy transfer to the Nd^{3+} ion would have a lifetime of less than 300 ps, corresponding to an intersystem crossing rate of $>1.6\times10^9$ s^{-1}, which would indeed explain the absence of a concentration quenching effect for these complexes. The lissamine complexes without energy transfer to the Nd would then have a luminescence lifetime of 0.6 ns. The fact that this lifetime is shorter than that measured for the same complexes in the solution (2.6 ns) is probably due to the concentration quenching which reduces the luminescence lifetime.

IV. PUMPING PLANAR WAVEGUIDE AMPLIFIERS USING A COUPLED WAVEGUIDE SYSTEM

A. Introduction

The pumping of optical waveguide amplifiers is usually done by coupling the pump beam into the waveguide at the input facet of the waveguide (butt coupling). The pump light is absorbed by the rare-earth ions as it travels through the waveguide, resulting in a decrease in pump power along the waveguide. In order to maintain sufficient pump power over the entire length of the waveguide, relatively high pump powers are coupled into the input section of the waveguide. This pumping scheme can be successfully used for materials in which high pump powers do not effect the pumping efficiency. However, in several materials systems an optimum pump power for amplification exist. Such systems include highly Er-doped waveguides in which cooperative upconversion and excited state absorption take place,[1] or systems in which the rare earth ions are excited via energy transfer from a sensitizer,[32,42] such as described in Section III. In these systems, butt–end coupling is not efficient. The excess pump power at the beginning of the waveguide will result in pump absorption that does not contribute to the optical gain.

In this section, we introduce a coupling configuration that can distribute the pump power evenly over the full length of the (signal) waveguide. It is based on the coupling between two waveguides in close proximity. In this scheme, the pump light is gradually coupled from a nonabsorbing pump guide into the adjacent amplifier guide. By gradually increasing the coupling (i.e., reducing the distance between the guides), it is possible to maintain a constant pump power along the signal guide. We will study the coupling between two parallel waveguides using coupled mode theory. A numerical example is given that shows that the optical gain of a sensitized Nd-doped polymer waveguide amplifier can be enhanced using this pump scheme.

B. Coupled mode theory for dissimilar waveguides

The waveguide structure under consideration is shown in Fig. 21. It consists of a pump waveguide A and a signal waveguide B. In order to evaluate the performance of this

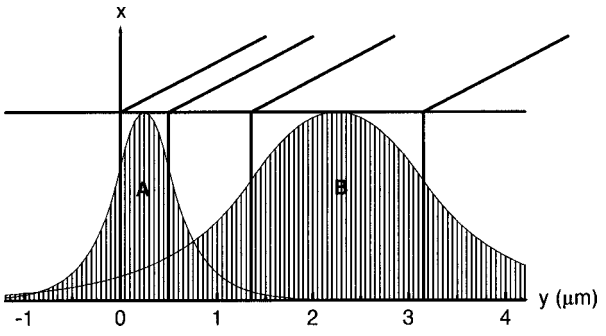

FIG. 21. Schematic presentation of a 2D coupled waveguide system consisting of parallel optical waveguides A and B. The calculated waveguide mode intensity along the x axis is shown for the waveguide geometry described in the text (515 nm pump A, 1.340 μm signal B).

system, we first need to calculate the coupling of pump power into the signal waveguide. This can be done using coupled mode theory.

The conventional coupled mode theory[43,44] deals with the coupling between two weakly interacting, nearly identical optical waveguides. The total field of the waveguide system can be written as a linear superposition of the individual waveguide modes $\mathbf{E}^a(x,y)$ and $\mathbf{E}^b(x,y)$:

$$\mathbf{E}=a(z)\mathbf{E}^a(x,y)+b(z)\mathbf{E}^b(x,y),$$
$$\mathbf{H}=a(z)\mathbf{H}^a(x,y)+b(z)\mathbf{H}^b(x,y), \tag{7}$$

with z the propagation direction. The coupled mode equations, defining the mode amplitudes $a(z)$ and $b(z)$ along the waveguide are given by

$$\frac{d}{dz}a(z)=i\gamma_a a(z)+ik_{ab}b(z),$$
$$\frac{d}{dz}b(z)=ik_{ba}a(z)+i\gamma_b b(z), \tag{8}$$

in which $\gamma_{a,b}$ are propagation constants and $k_{ab,ba}$ are mutual coupling constants which in this case are identical. If the waveguides are not identical, or in the case of strong coupling, the mutual coupling coefficients are different for the two waveguides, and as a result power is not conserved in the conventional theory. This problem can be dealt with using modified propagation and coupling parameters γ_a, γ_b, k_{ab}, and k_{ba}, as given in appendix A.[45] These parameters are known nonlinear functions of the fields of the unperturbed individual waveguide modes. Consequently, when the unperturbed modal solutions for the individual waveguides are known, the fields of the coupled waveguide system can be calculated.

The optical modes of the individual waveguides are a solution to the (Helmholtz) wave equation and can be derived from Maxwell's equations. In principle, one should take into account the complete two-dimensional field pattern over the cross section of the waveguide. However, in good approximation the field $\mathbf{E}(x,y)$ can be written as $\mathbf{E}(x)\times\mathbf{E}(y)$. In this approximation, it can be easily shown that if the waveguides have the same thickness (defined in the x direction, see Fig. 21), the coupling only depends on $\mathbf{E}(y)$. Using the correct boundary conditions, the transverse electric (TE) field pattern for the first even mode of the pump waveguide A is given by:

$$E^a(y)=C_a\begin{cases}\cos\left(k_y\frac{d}{2}\right)e^{-\alpha(y-d/2)} & y\geqslant+\frac{d}{2}\\ \cos(k_y y) & |y|\leqslant\frac{d}{2}\\ \cos\left(k_y\frac{d}{2}\right)e^{+\alpha(y+d/2)} & y\leqslant-\frac{d}{2}\end{cases}, \tag{9}$$

in which k_y and α are determined from the eigenvalue equation, which is obtained by substituting Eq. (9) into the wave equation, C_a is a normalization constant, and d the waveguide width. This calculation can also be done to obtain the TE field of the signal guide B.

With the modal fields of Eq. (9) as input for the coupled mode equations of Eq. (8), the modal amplitudes $a(z)$ and $b(z)$ can be calculated. If all pump power is launched into waveguide A at $z=0$ $[a(0)=1,b(0)=0]$, the solution can be written as[46]

$$a(z)=\left(\cos(\psi z)-i\frac{\Delta}{\psi}\sin(\psi z)\right)e^{i\varphi z}$$
$$b(z)=i\frac{k_{ba}}{\psi}\sin(\psi z)e^{i\varphi z}, \tag{10}$$

where

$$\varphi=\frac{\gamma_a+\gamma_b}{2}$$
$$\psi=\sqrt{\Delta^2+k_{ab}k_{ba}} \tag{11}$$
$$\Delta=\frac{\gamma_b-\gamma_a}{2}.$$

We can now calculate the pump power coupled into the signal guide B:

$$P(z)=\frac{1}{2}\mathrm{Re}\int\int\mathbf{E}\times\mathbf{H}^*\cdot\hat{\mathbf{z}}dxdy$$
$$=|a(z)|^2+|b(z)|^2+\mathrm{Re}[a(z)b^*(z)C_{ba}+b(z)a^*(z)C_{ab}], \tag{12}$$

where the cross overlap integrals C_{ab} and C_{ba} are given by

$$C_{ab}=\frac{1}{2}\int\int\mathbf{E}^b\times\mathbf{H}^a\cdot\hat{\mathbf{z}}dxdy,$$
$$C_{ba}=\frac{1}{2}\int\int\mathbf{E}^a\times\mathbf{H}^b\cdot\hat{\mathbf{z}}dxdy, \tag{13}$$

and the integration is done over the cross section of the signal waveguide.

Using the same set of equations, it is also possible to calculate the coupling of the signal mode into the pump guide. In the present waveguide geometry (a broad single-mode signal guide and a narrow single-mode pump guide), this loss can be neglected.

TABLE III. Waveguide parameters of the coupled optical waveguide system as used in the calculation.

Guide	λ (nm)	n_{guide}	k_{guide}	$n_{cladding}$	$k_{cladding}$
Pump	515	1.5067	0	1.4616	0
	1340	1.4845	0	1.4465	0
Signal	515	1.4973	0.0125	1.4616	0
	1340	1.4831	0	1.4465	0

C. Numerical example

Using the equations derived herein, we can now calculate the effect of distributed coupling. As an example, we will consider the sensitized Nd^{3+}-doped polymer waveguide described in Sec. III. The Nd ions are incorporated in an organic complex that also contains an organic sensitizer group. In these complexes, 1340 nm emission of Nd is observed after excitation via the lissamine sensitizer. In this way, the Nd^{3+} ion can be excited efficiently, as a result of the high absorption of the lissamine at the pump wavelength (515 nm). However, if the pump power is higher than the value needed for complete population inversion of the Nd, the excess pump light is absorbed by the lissamine, leading to a reduced pumping efficiency. Therefore, the pump power should be kept below a certain limit over the length of the waveguide.

In this example, the pump power ($\lambda = 515$ nm) is coupled through a 0.5 μm wide waveguide parallel to a 1.8 μm wide signal ($\lambda = 1340$ nm) waveguide at a spacing between the centers of the waveguide of 2 μm. Both waveguides support only the fundamental mode (see Fig. 21). The real (n) and imaginary (k) part of the refractive index are listed in Table III for the two waveguides. In the present geometry, coupling from the signal waveguide into the pump waveguide is negligible, as the narrow pump guide does not support the 1340 nm mode. To avoid contamination of the pump waveguide with the sensitized Nd^{3+}-complex, the doped waveguide should be made first. This can be done by spincoating the doped layer onto the cladding layer in which the signal waveguide is etched. Next, the surplus of film is etched away, followed by the etching of the second trench for the pump waveguide. This can than be filled with the undoped polymer by a second spincoat step.

Figure 22 shows the calculated intensity distribution of the pump over the length of the waveguide, using an input pump power of 1 W. The intensity decrease in the nonabsorbing pump guide is entirely due to absorption of pump light coupled into the highly absorbing signal waveguide. In the present configuration, the pump power is almost completely absorbed after a distance of about 4 cm. The pump power in the signal guide as a function of the distance follows the same decreasing trend, as the coupling constant is constant over the length of the waveguides. It is not visible on the scale of Fig. 22, as the coupling constant is very small. It can be determined by integrating the data in Fig. 22 across the signal waveguide. The result is shown in Fig. 23. As can be seen, the power in the signal guide decreases from about 6 mW to almost zero over a distance of 4 cm.

The Nd^{3+} system can be described by a four-level system, in which there is no minimum pump power required for optical gain. The differential gain along the amplifier is calculated using the known rate equations for the Nd^{3+} level system, which are given in appendix B, and the pump power as a function of distance along the guide calculated herein. Table IV gives the values for the different rates used in the optical gain calculation. The result is shown in the inset of Fig. 23. Note that even with a pump power as low as 0.6 mW at the beginning of the signal guide, the differential gain is still reasonably high (~1.6 dB/cm). The total optical gain for this waveguide amplifier is given by

$$\text{gain(dB)} = 4.34 \times \eta \times \left(\int_0^L \sigma_{se} N f(z)\, dz \right), \tag{14}$$

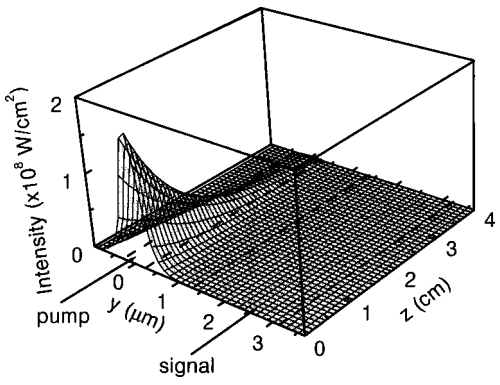

FIG. 22. Pump intensity in the waveguide structure as a function of distance z along the waveguide.

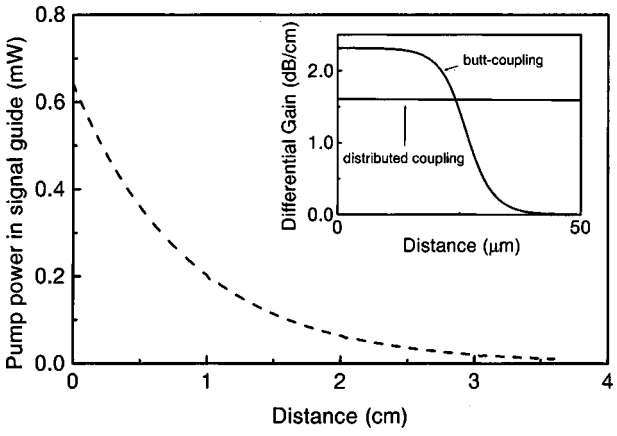

FIG. 23. Pump power in the signal guide as function of distance z in a sensitized Nd-doped polymer waveguide. The inset shows the calculated differential gain as a function of distance along the waveguide for a coupled waveguide system, and a butt–coupled waveguide. The input power in the pump waveguide is 1 W in both cases.

TABLE IV. Values for the different rates used in the optical gain calculation for distributed coupling. $P(W)$ is the pump power in the signal guide. The values of the different rate constants have been derived from spectroscopic measurements described in Sec. III except from W_{et}, which is estimated from oxygen quenching experiments [22] and W_{s2} which is an estimate based on typical triplet state lifetimes.

Rate	W_p (s^{-1})	W_{s1} (s^{-1})	W_{s2} (s^{-1})	W_{isc} (s^{-1})	W_{et} (s^{-1})	W_{40} (s^{-1})
Value	$5\times10^9\ P(W)$	4×10^8	10^4	4.3×10^8	10^8	10^6

in which $\sigma_{se}=1\times10^{-20}$ cm^2 is the cross section for stimulated emission at 1340 nm,[47–49] $N=5\times10^{19}$ cm^{-3} is the Nd^{3+} concentration, $f(z)$ is the fraction of excited Nd (see appendix B), L is the length of the waveguide, and $\eta=78\%$ is the relative overlap between pump and signal mode in the signal waveguide. For the example given, the total gain is calculated to be 1.6 dB for a 4 cm long waveguide amplifier. To show the effect of distributed coupling, the inset of Fig. 23 also includes the differential gain obtained by using conventional butt coupling at the same input pump power of 1 W. Note that all pump power is completely absorbed within the first 50 μm. The maximum gain for this case is only 0.005 dB. Note that we have not taken into account the intrinsic waveguide losses at 1340 nm (~0.2 dB/cm).[3]

Figure 24 shows the effect of the distance between two parallel 4 cm long waveguides on the differential gain. If the distance between the waveguides decreases, the coupling becomes stronger as more pump power will be coupled into the signal guide. This results in a higher differential gain at the beginning of the signal guide, but the pump power will be consumed more rapidly. Besides that, the pump power at the beginning of the waveguide is higher than the pump power for maximum amplification, resulting in pump losses. As a result, the total integrated optical gain will be lower. This can be seen in the inset of Fig. 24, which shows the total integrated optical gain for a 4 cm long waveguide coupler as a function of the distance between the waveguides. For a larger separation between the waveguides, the coupling is smaller, less pump power is coupled into the signal guide and the differential gain is lower. In this configuration, the total integrated optical gain is lower, but not all pump power is consumed. If the waveguide coupler is made longer, such that all pump power is used, the total integrated optical gain will be similar as for the 4 cm long coupler with the optimum separation of 2.1 μm between the guides.

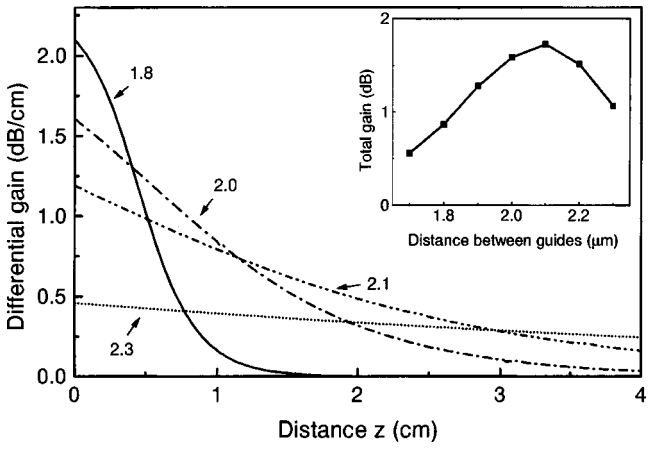

FIG. 24. Differential gain over the length of the waveguide, plotted for different separation between the waveguides. The numbers in the plot indicate the waveguide separation in μm. The inset shows the total gain for 4 cm long pump and signal waveguides as a function of the waveguide separation.

V. ERBIUM-IMPLANTED SILICA COLLOIDS

A. Introduction

In Secs. II and III, we have investigated organic rare-earth complexes which can be dissolved in a polymer matrix.[20,42,50] Both for Er and Nd, it was observed that coupling to vibrational overtones of C—H or O—H bands strongly quenches the luminescence.[16,21] However, it is known that SiO_2 is an excellent host for rare-earth ions, yielding long luminescence lifetimes.[10,13] It would therefore be interesting to study if the easy processing of polymers could be combined with the long luminescence lifetime of Er in silica. In this section, we study the optical doping of colloidal silica particles using Er ion implantation. The influence of Er concentration and anneal temperature on the luminescence intensity and lifetime is determined. It is found that the silica colloids are an excellent host for Er, yielding a high quantum efficiency. As a first demonstration of the possible application in polymer waveguides, optical transmission measurements are shown for a polymer film doped with these silica colloids.

B. Colloid preparation

Silica colloids with a diameter of 244 or 360 nm were synthesized as described by van Blaaderen *et al.*[51] Solutions of 10 ml ethanol, 0.7 ml NH_3 (28 wt. % in water), 0.8 ml H_2O and 0.4 ml tetraethoxysilane [(TEOS) 99%] were mixed and stirred for 1 h at room temperature, resulting in nucleation and growth of silica colloids with a diameter of 244 $\pm$10 nm, as measured using scanning electron microscopy (SEM). In one set of samples, the diameter of the spheres was increased to 360 nm by subsequent addition of TEOS to the reaction vessel.[52] After the reaction, the suspension was centrifuged and the remaining colloids were dissolved in pure ethanol. Droplets of the solution were put onto a silicon substrate or a microscope cover glass (cleaned with a 1 M KOH/ethanol solution). After evaporation of the ethanol, a thin layer of colloids remained. Next, the samples were irradiated with 350 keV Er^+ ions at various fluences ranging from 0.9×10^{15} to 5.5×10^{15} ions/cm^2. The projected range of 350 keV Er^+ in silica is 160 nm. Implantation of these ion fluences into a planar film results in a Gaussian Er distribution with a FWHM of 34 nm. It is obvious that in these

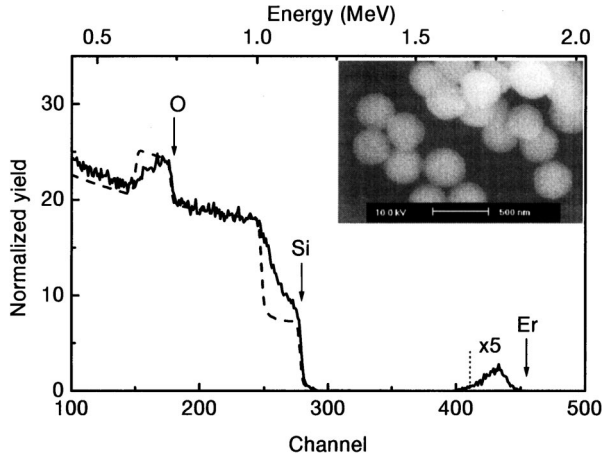

FIG. 25. RBS spectrum of a single layer of Er-implanted (350 keV and 9×10^{15} Er/cm^2) silica colloids on a Si substrate (solid line). 2 MeV He^+ ions were used at a scattering angle of 165°. A simulation of a 360 nm SiO_2 film on a silicon substrate (dashed line) is also shown. The dashed line at channel 410 indicates the position of the SiO_2/Si interface for Er. The inset shows a SEM image of the same sample.

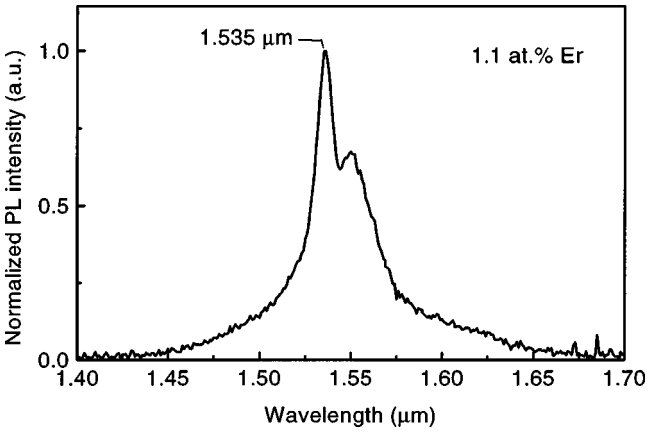

FIG. 26. PL spectrum for a thick layer of silica colloids, implanted with Er (1.1 at. %), taken using 515 nm pump light at a power density of 60 mW/mm^2.

nonuniform, colloidal layers a less well-defined concentration profile builds up. After implantation, the samples were annealed in vacuum at 100 °C for 1 h and then for another hour at different temperatures in the range 700 °C–1000 °C.

In order to study the Er incorporation in the colloids, Rutherford backscattering spectroscopy (RBS) measurements were performed, using a 2 MeV He^+ beam at a scattering angle of 165°. SEM was performed at an electron energy of 10 keV. Optical transmission measurements were performed at normal incidence using a spectrometer at wavelengths ranging from 300–1700 nm.

C. Results and discussion

Figure 25 shows a RBS spectrum of a Si sample covered with a single layer of 360 nm diameter colloids, implanted with 9×10^{14} Er/cm^2. For reference, a simulation of a 360 nm pure SiO_2 layer on a Si substrate is also shown (dashed line). The surface channels of Er, Si, and O are indicated by the arrows. The Si content at the surface is almost similar to the Si content in pure SiO_2, indicating that the substrate is almost completely covered with colloids. The Si yield then increases with decreasing energy, as a result of the spherical shape of the colloids. The Si yield coincides with that of the simulation at channel 245, consistent with the colloid diameter of 360 nm. The signal between channel 400 and 500 is due to the implanted Er. The Er peak concentration is 0.18 at. %. Note that a small fraction of the implanted Er has entered the Si substrate, as is evident from the Er tail near channel 400. The inset in Fig. 25 shows a SEM image of deposited colloids (360 nm diameter), showing a rather disordered array of particles extending over several layers.

The samples used for PL measurements consisted of about three to four layers of silica colloids, as determined from RBS and SEM. Figure 26 shows the PL spectrum of colloidal silica particles implanted to a peak concentration of 1.1 at. % and annealed at 950 °C for 1 h. SEM showed that the implantation and annealing caused no deformation of the silica spheres. The spectrum shows typical Er^{3+} luminescence around 1.53 μm due to transitions from the $^4I_{13/2}$ to the $^4I_{15/2}$ level. The two peaks result from Stark splitting of the Er^{3+} levels and are characteristic for Er^{3+} in SiO_2.[50] The width (32 nm FWHM) is due to the thermal distribution over the Stark levels as well as inhomogeneous broadening. It is difficult to compare PL intensities for different implanted samples as the colloid coverage varies from sample to sample, and because of the fact that the pump beam is strongly scattered by the silica spheres, which results in nonuniform pumping. However, on average the intensity increases for increasing doping concentration up to at least 1.1 at. % (data not shown).

Figure 27(a) shows the peak PL intensity of samples implanted with 0.2 at. % Er, annealed at various temperatures for 1 h. Below 700 °C, no measurable PL was observed. This

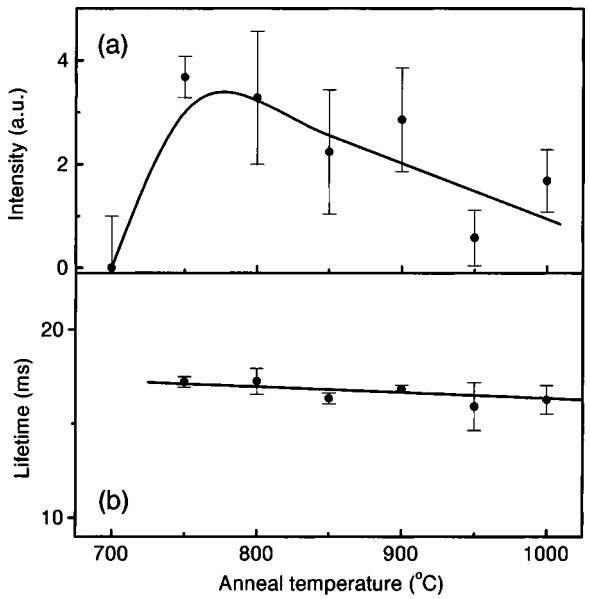

FIG. 27. (a) Average peak PL intensity at 1.53 μm as a function of anneal temperature for Er-implanted silica spheres (0.2 at. %). Pump wavelength 488 nm, pump power 50 mW. The large error bars are due to the large variation in colloid coverage over the surface. (b) Luminescence lifetime of Er-implanted silica spheres (0.2 at. %) as a function of anneal temperature.

might be due to water that is physisorbed on the surface or trapped in the pores of the silica matrix. Water is known to quench the Er^{3+} luminescence, as the first overtone of the O—H vibration ($E_0 = 3400\ cm^{-1}$) is strongly resonant with the Er^{3+} transition ($E = 6500\ cm^{-1}$). Indeed, work by Fan *et al.*[53] and Tien *et al.*[54] on bulk silica samples, grown in a similar way as the colloids, shows that between room temperature and 200 °C, weakly bound water and residual organic molecules vaporize, followed by the removal of chemically bound molecular water between 300 °C and 800 °C. Figure 27(a) shows large scatter in the data above 700 °C, but the general trend is a decrease in PL intensity, certainly for temperatures above 900 °C. This may be due to the precipitation of Er, as has been observed before in Er-implanted SiO_2.[10] Figure 27(b) shows luminescence lifetime measurements as a function of anneal temperature for an Er concentration of 0.2 at. %. For anneal temperatures below 700 °C, the PL intensity was too low to perform lifetime measurements. The lifetime for anneal temperatures between 750 and 1000 °C is about 17 ms and is almost independent of anneal temperature.

We have also performed lifetime measurements for samples implanted at higher doses, and found that increasing the Er concentration from 0.2 to 1.1 at. % results in a decrease in the luminescence lifetime from 17 to 10 ms. These lifetimes are among the highest we have observed in silica glass. Assuming that the decrease in lifetime is due to concentration quenching, we can estimate the radiative lifetime by linearly extrapolating to zero Er concentration[55] and find $\tau_{rad} = 20-22$ ms. The long lifetimes observed in this work show that silica glass made by wet chemical synthesis is an excellent host for Er. It indicates that the water impurity content in this glass after annealing is very small (<1 ppm).[56] We note that the long radiative lifetime can be partly attributed to the fact that the Er-implanted colloids are surrounded by air and are relatively far away from the high-index Si substrate, causing the local optical density of states in the colloids to be lower than that of bulk SiO_2.[13,57] This will be further discussed in Sec. VI.

Two months after the first PL measurements on the Er-implanted colloidal particles, we performed the same measurements again and found that the luminescence intensity and lifetime were strongly reduced. After annealing at 475 °C, both the luminescence intensity and lifetime returned to the level observed after the initial anneal. This suggests that some time after the anneal, a thin film of water covers the colloids. This makes it necessary to coat the silica spheres with a protective layer, e.g., a polymer.

In order to investigate the application of these colloids in polymer waveguides, undoped silica colloids with a diameter of 244 nm were deposited onto a microscope cover glass. Next, the samples were annealed for 1 h at 100 °C, and subsequently a solution of 1.5 g PMMA in 10 ml chloroform was spun onto the substrate at a spinrate of 2000 rpm for 30 s, resulting in a 1 μm thick film. An optical transmission measurement on this colloid/polymer nanocomposite film is shown in Fig. 28 as the dotted line. For reference, a spectrum of the glass substrate is shown (dashed line), together with the transmission spectrum of the substrate covered with

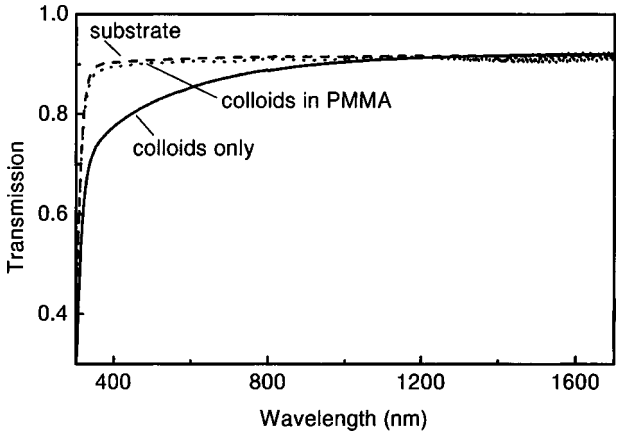

FIG. 28. Optical transmission measurements of a 1 μm silica/polymer nanocomposite film on a microscope cover glass (dotted line) and of a cover glass with colloids only (solid line). Measurements are also shown for a bare cover glass (dashed line).

silica spheres (without polymer, solid line). As can be seen, without the polymer coating, the transmission at short wavelengths is strongly reduced due to scattering by the silica spheres. Covering the spheres ($n = 1.43$) with a PMMA ($n = 1.48$) layer reduces the scattering by reducing the refractive index difference between the SiO_2 colloids and its surroundings. Note that in this measurement, the interaction length is only ~ 1 μm. In a homogeneously doped polymer waveguide with a length of a few cm, the effect of scattering will be stronger. This will be discussed in the next section.

D. Performance estimate of a polymer/colloid nanocomposite waveguide amplifier

1. Calculation of scattering losses

Er-doped silica spheres can be coated with alkoxy groups, which make them soluble into a polymer layer. These polymer-colloid nanocomposite layers can then be used in a polymer based optical amplifier operating at 1.5 μm. For this kind of application, it is important that the Er-doped layers have very low intrinsic losses. One loss component may be caused by the refractive index mismatch between colloid and polymer. In the Rayleigh limit, where the colloid radius r is smaller than the wavelength, the scattering cross section of a colloid with refractive index n_c embedded in a medium with refractive index n_m is given by

$$C_{sca} = \frac{8}{3}\left(\frac{2\pi n_c r}{\lambda}\right)^4 \cdot \left(\frac{\left(\frac{n_c}{n_m}\right)^2 - 1}{\left(\frac{n_c}{n_m}\right)^2 + 2}\right)^2 \pi r^2. \tag{15}$$

The total scattering coefficient is then given by

$$a_{sca} = \frac{3\eta C_{sca}}{4\pi r^3}, \tag{16}$$

where η is the fill fraction of the spheres in the polymer host.

Figure 29 shows the scattering loss per unit length as a function of sphere radius for a typical case, i.e., a polymer refractive index of $n_m = 1.48$ (typical for PMMA at 1.5 μm), and $n_c = 1.45$ for the silica spheres, and a fill fraction of 0.6.

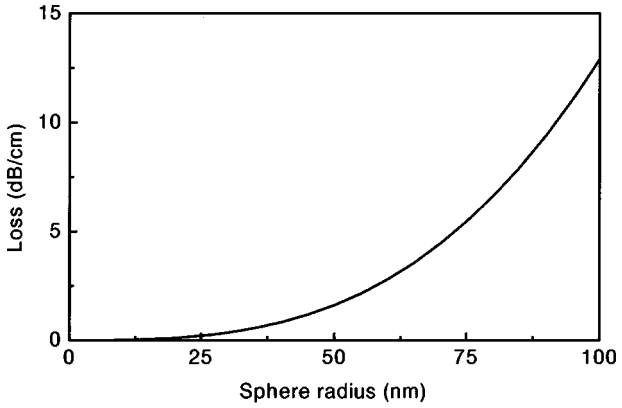

FIG. 29. Scattering loss per unit length as a function of sphere radius for SiO_2 spheres ($n=1.45$) embedded in a PMMA film ($n=1.48$).

As can be seen, the scatter loss rapidly increases for increasing particle size, and (for this particular index mismatch) the sphere radius should be kept below ~40 nm in order to keep the scattering losses below 1 dB/cm.

Figure 30 shows the maximum particle radius as a function of index mismatch, that is calculated to yield a waveguide loss of 0.1 dB/cm. As can be seen, for a particle with a radius of 50 nm, the refractive index difference has to be kept below ~0.008. One should also keep in mind that the dependence of refractive index on temperature is different for the SiO_2 and the polymer. An increase of 100 °C in temperature results in a relative index difference of 0.02 as calculated using the Clausius–Mossotti relation and the known thermal expansion coefficients of the polymer and SiO_2. As can be seen in Fig. 30, this means that the maximum particle radius has to be about 25 nm, in order to keep the scattering losses below 0.1 dB/cm over a temperature range of 100 °C. The data in Figs. 29 and 30 illustrate that the refractive index of the polymer must be matched very precisely.

2. Optical gain

Assuming that the waveguide loss due to scattering can be eliminated, an estimate of the optical gain for an Er-doped silica sphere/polymer nanocomposite optical waveguide can

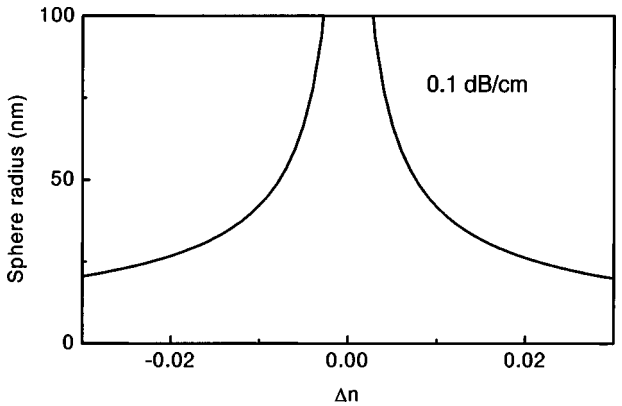

FIG. 30. Maximum sphere radius as a function of refractive index mismatch Δn between the polymer layer and SiO_2 spheres, yielding a scattering loss of 0.1 dB/cm.

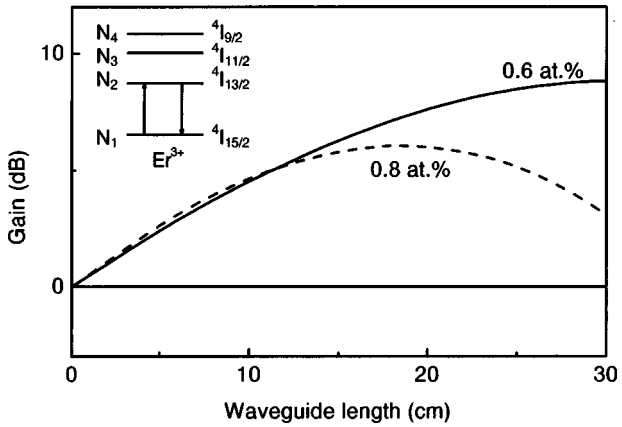

FIG. 31. Total gain as a function of waveguide length for an Er-doped colloid/polymer composite waveguide amplifier pumped at 1.48 μm. Data are shown for Er concentrations in the colloid of 0.6 at. % (solid line) and 0.8 at. % (dashed line), at an input power of 20 mW. The inset shows a schematic energy diagram of Er^{3+}. The notation on the right-hand side shows the Russel–Saunders notation of the different levels, whereas the notation on the left-hand side shows the symbols as used in the rate equations of Eq. (7.4).

be made. The optical gain as function of the waveguide length L is calculated using the following equation:

$$\text{gain(dB)} = 4.34 \times \int_0^L (\sigma_{21s} N_2 - \sigma_{12s} N_1 - \sigma_{24} N_2)\, dz, \tag{17}$$

in which σ_{21s} and σ_{12s} are the cross sections for stimulated emission and absorption at the signal wavelength ($\lambda = 1535$ nm), σ_{24} is the signal excited state absorption cross section, and N_1 and N_2 are the populations of the ground and first-excited state of the Er^{3+} ion, respectively (see inset Fig. 31). These populations are obtained by solving the following rate equations for steady state conditions, and include the effect of cooperative upconversion,[58–61] in which two neighboring excited Er^{3+} ions interact and exchange energy, as well as excited state absorption,[62,63] in which an Er^{3+} ion in the N_2 level absorbs a pump photon, exciting it into the N_4 level:

$$\begin{aligned}
&\frac{dN_1}{dt} = -R_{12}N_1 + R_{21}N_2 + \frac{N_2}{\tau_2} + C_{24}N_2^2 = 0\\
&\frac{dN_2}{dt} = R_{12}N_1 - R_{21}N_2 - \frac{N_2}{\tau_2} + \frac{N_3}{\tau_3} - 2C_{24}N_2^2 - R_{24}N_2 = 0\\
&\frac{dN_3}{dt} = -\frac{N_3}{\tau_3} + \frac{N_4}{\tau_4} = 0,\\
&\frac{dN_4}{dt} = -\frac{N_4}{\tau_4} + C_{24}N_2^2 + R_{24}N_2 = 0\\
&N_1 + N_2 + N_3 + N_4 = N
\end{aligned} \tag{18}$$

where N_i are the Er^{3+} populations in the first four energy levels (see inset Fig. 31), N is the total Er^{3+} concentration, τ_i is the luminescence lifetime of state N_i, R_{12} is the pump rate, R_{21} is the rate of stimulated emission by the pump, R_{24} is the excited state absorption rate, and C_{24} is the coefficient for cooperative upconversion. The rates R_{ij} are equal to

TABLE V. Parameters and their symbols as used in the optical gain calculation for the Er-doped silica sphere/polymer nanocomposite optical waveguide amplifier.

Parameter	Symbol	Value
refractive index of sphere	n_c	1.45
refractive index of medium	n_m	1.45
pump wavelength	λ	1.480 μm
pump absorption corss section[a]	σ_{12}	1.0×10^{-21} cm^2
pump emission cross section[a]	σ_{21}	0.5×10^{-21} cm^2
signal absorption cross section[a]	σ_{12s}	4.1×10^{-21} cm^2
signal emission cross section[a]	σ_{21s}	5.0×10^{-21} cm^2
upconversion coefficient[b]	C_{24}	3.2×10^{-18} cm^2/s
excited state absorption cross section[c]	σ_{24}	0.5×10^{-21} cm^2
luminescence lifetime level 2[d]	τ_2	$0.8\times(48+64\times N_{at})^{-1}$ s
luminescence lifetime level 3[e]	τ_3	10^{-6} s
luminescence lifetime level 4[a]	τ_4	10^{-9} s
erbium concentration in spheres	N_{at}	0.4 at. %
fill fraction of spheres/medium	η	0.6
atomic density of SiO_2	ρ	6.60×10^{22} at/cm^3
total erbium concentration	N	$\eta\times N_{at}\times\pi$ at/cm^3
input pump power	P_0	5 mW
waveguide cross section	a	2.56×10^{-8} cm^2
mode overlap	η	40%
waveguide loss		0 dB/cm

[a]See Ref. 66.
[b]See Ref. 61.
[c]See Ref. 67.
[d]See Ref. 68.
[e]See Ref. 69.

$(\sigma_{ij}P\lambda)/(hca)$, with σ_{12} and σ_{21} as the absorption and stimulated emission cross sections at the pump wavelength ($\lambda=1480$ nm), σ_{24} as the excited state absorption cross section, h as Planck's constant, c as the speed of light, a as the waveguide cross section, η as the mode overlap with the waveguide core, and P as the pump power along the length of the waveguide.

Calculating P over the length of the waveguide, the populations of the ground state and first excited state can be calculated over the entire waveguide. These populations are then put into Eq. (17) in order to calculate the optical gain. The parameters used in the calculation are given in Table V. Cross sections and lifetimes were taken from earlier work on Er-implanted silica glass. The expression for τ_2 in Table V includes the effect of concentration quenching as will be discussed in the next section, and a factor 0.8 for the change in decay rate relative to the decay rate measured on Er-implanted colloids because of the enhanced local density of states due to the presence of the polymer (see Sec. VI C). The waveguide cross section was chosen such that it supports the first-order mode in a waveguide based on a SiO_2 sphere doped PMMA guiding layer ($n=1.45$) and a fluorinated PMMA cladding layer ($n=1.37$). Note that due to the high index contrast that can be achieved using polymers, very well confined optical modes can be achieved, leading to a low pump threshold for optical gain. Figure 31 shows the calculated optical gain as a function of the length of the waveguide for two different Er concentrations at a pump power of 20 mW. As can be seen, for a given Er concentration, the gain first increases, reaches a maximum, and then decreases again. This is due to the fact that at the entrance of the waveguide the pump power is high enough to create population inversion between the first excited state and the ground state, but as the pump power decreases along the length of the waveguide, due to absorbing Er^{3+} ions, at some point the pump power is no longer sufficient to create population inversion, resulting in net absorption. The higher the Er^{3+} concentration, the shorter the waveguide length at which maximum gain is achieved. The fact that a lower maximum gain is achieved for the higher concentration is due to the effect of cooperative upconversion at high concentration.

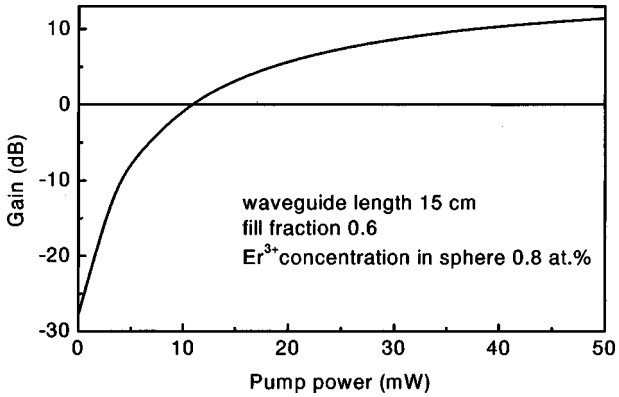

FIG. 32. Total gain at 1.535 μm as a function of input pump power for a 15 cm long waveguide amplifier at an Er concentration of 0.8 at. %.

Next, the optical gain was calculated as a function of pump power for an Er^{3+} concentration of 0.8 at. % and an amplifier length of 15 cm. The result is shown in Fig. 32. At zero-pump power, the Er^{3+} ions only absorb and no population inversion is established, resulting in negative gain. At a pump power of about 10 mW, population inversion is reached and optical gain is achieved. Further increasing the pump power to 50 mW results in a maximum optical gain of 12 dB. Note that at a given pump power, the optical gain in these silica colloid/polymer amplifiers is much higher than that in a pure silica waveguide amplifier. This is due to the fact that in this design, a large index contrast between polymer cladding and core can be chosen, leading to high mode confinement. This high index contrast also enables waveguide bends with relatively small bending radii so that by using the proper spiral geometry,[1] a 15 cm long waveguide amplifier can be rolled up to a size of only 16 mm^2.

VI. MODIFIED SPONTANEOUS EMISSION IN ERBIUM-DOPED SiO_2 SPHERICAL COLLOIDS

A. Introduction

Er-doped dielectric materials find many applications in optical components, due to their sharp optical emission at 1.5 μm, the standard wavelength in optical telecommunications technology. Recently, Er-doped colloids[64] and microspheres[65] have been investigated. Small ($\sim$100 nm diameter) colloids can find applications in nanocomposite materials that can be used to fabricate a polymer optical amplifier (see Sec. V), while larger colloids or microspheres (>10 μm) can be used to fabricate whispering gallery mode lasers

operating at 1.5 μm. Optically active colloids can also find applications as probes in photonic crystals, in which they can be used to probe the (local) optical density of states.

Two important parameters determine the gain performance of Er-doped colloids: the stimulated emission cross section and the emission quantum efficiency. The Er^{3+} intra-$4f$ transitions at 1.53 μm are, in principle, forbidden by the parity selection rule, but mixing with other-parity states makes them slightly allowed. Hence, the transitions have a relatively small optical cross section, and consequently, the excited state of Er^{3+} has a long luminescence lifetime.

For a given material, a measurement of the luminescence lifetime can be made relatively easily, thus providing a quick identification of the emission cross section. However, in practice the lifetime is not only determined by radiative emission, but also by nonradiative processes such as multiphonon relaxation, coupling to defects, or interactions between Er ions,[70,71] that can all quench the excited state. Furthermore, the radiative emission rate is not a fixed property for a given material, but depends on the optical surrounding of the Er ions. For example, the presence of dielectric boundaries changes the local electric field fluctuations and modifies the spontaneous emission rate.[57,72] Changes in decay rate can be determined by calculating the local optical density of states (DOS) and then applying Fermi's Golden Rule. The radiative decay rate can then be written in terms of a local DOS $\rho(\omega,r)$ as:

$$W_{\mathrm{rad}}(\mathbf{r}) = \frac{\pi\omega}{\hbar\,\epsilon(\mathbf{r})}|D|^2\rho(\omega,\mathbf{r}), \tag{19}$$

where $\epsilon(\mathbf{r})$ is the position-dependent dielectric constant, ω is the transition frequency, and $|D|^2$ is the dipole matrix element of the transition involved. This matrix element is determined by the interaction of Er^{3+} ions with the coordinating matrix, while the macroscopic $\rho(\omega,\mathbf{r})$ and $\epsilon(\mathbf{r})$ are determined by the optical surroundings.

In this section, we study the modified spontaneous emission of Er ions implanted into spherical SiO_2 colloids. In such small particles, there is a strong interaction between excited Er ions and the colloid–air interface. Using a combined analysis of concentration quenching phenomena and DOS effects in colloids with two different diameters, we are able to determine absolute values of the radiative and nonradiative decay rates. We find that the spontaneous emission rate for the two sizes differs by 50% and determine the emission cross section.

B. Experiment

SiO_2 colloids with a diameter of either 175 or 340 nm ($\pm$5%) were made in a reaction between tetra-ethoxysilane, ammonia, ethanol, and water as described in Ref. 51. The spheres were deposited on Si(100) substrates that were cleaned for 15 min in a 1.0 M KOH solution in ethanol. A droplet of the spheres dissolved in ethanol was put on the substrate and the ethanol was left to evaporate. The 175 nm SiO_2 colloids were implanted at room temperature with 70 keV Er^+ ions to fluences of 3.4×10^{14} ions/cm^2 or 9.1×10^{14} ions/cm^2. The ion range of 70 keV Er in silica is $r=48$ nm, and the straggle $\sigma=11$ nm. The Er peak concentration is 0.2 or 0.5 at. % for the two fluences, respectively. The 340 nm colloids were implanted with 350 keV Er^+ ions ($r=160$ nm and $\sigma=34$ nm) at fluences of 9.0×10^{14}, 2.5×10^{15}, or 4.0×10^{15} ions/cm^2 (peak concentrations 0.2, 0.5, or 0.8 at. %). After implantation, the samples were annealed in a vacuum furnace (pressure $<5\times10^{-7}$ mbar) at 100 °C for 1 h and at 900 °C for another hour. The inset in Fig. 33 shows a SEM image of the 340 nm diameter colloids.

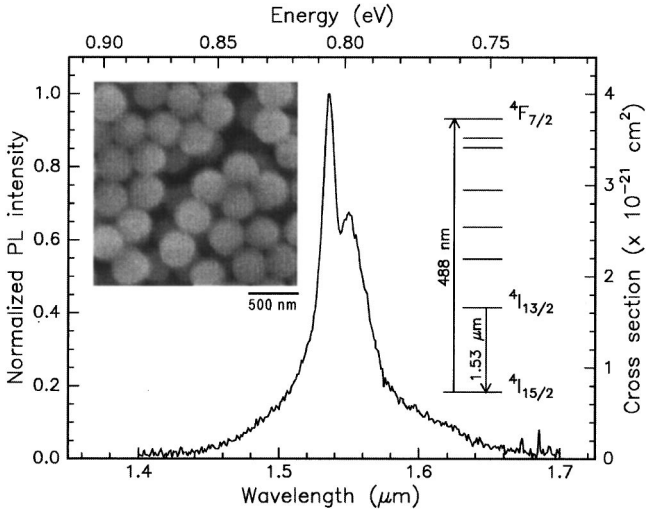

FIG. 33. PL spectrum of Er-implanted SiO_2 colloids (340 nm diameter, 0.2 at. % Er), measured at room temperature under 488 nm excitation. The inset shows a SEM image of 340 nm diameter colloids.

PL measurements were performed using excitation with the 488 nm line of an Ar ion laser. The pump beam was modulated at 13 Hz using an acousto-optic modulator. The PL signal was focused onto the entrance slit of a 48 cm grating monochromator and detected with a liquid-nitrogen cooled Ge detector employing standard lock-in techniques. The spectral resolution of the system was 6 nm. PL decay traces of the luminescence were recorded at the peak of the Er luminescence at 1.535 μm and averaged using a digitizing oscilloscope. The overall time response of the system was measured to be 30 μs. All decay traces showed single-exponential behavior.

C. Results and discussion

Figure 33 shows a PL spectrum of 340 nm colloids implanted to a peak concentration of 0.2 at. % Er. The Er ions are excited into the $^4F_{7/2}$ level as shown in the inset. The emission is due to transitions from the first-excited state ($^4I_{13/2}$) to the ground state ($^4I_{15/2}$), peaking at a wavelength of 1.535 μm. Figure 34 shows PL decay rates measured as a function of Er peak concentration for both the 175 nm colloids (open circles) and the 340 nm colloids (closed circles). For both diameters, the PL decay rate increases with Er concentration, an effect that is generally known as concentration quenching.[55,71] It is due to an increased coupling to quenching sites as a result of excitation migration at high Er concentration (see inset in Fig. 34). For example, in silica glasses it is well known that small quantities of OH impuri-

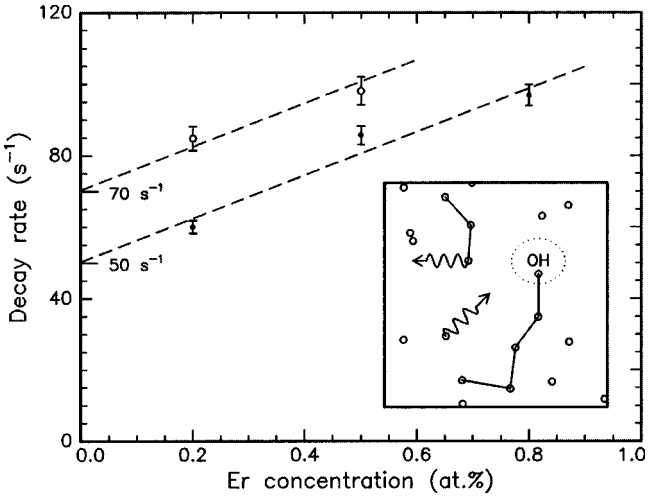

FIG. 34. PL decay rates measured at 1.535 μm for Er-implanted colloids as function of Er peak concentration. Data are shown for 175 nm colloids (open circles) and 340 nm colloids (closed circles). The dashed lines are fits to the data according to Eq. (20) assuming an identical slope for both data sets, but different vertical offsets. The inset shows a schematic of the concentration quenching process: excitation migration among Er ions followed by quenching at an OH impurity.

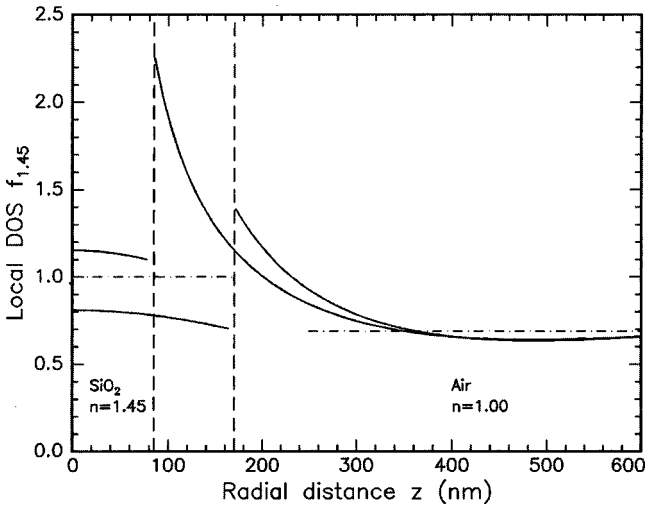

FIG. 35. Polarization-averaged local optical DOS as function of radial position for SiO_2 colloids ($n=1.45$) in air ($n=1.00$), calculated at a vacuum wavelength of 1.535 μm. Data are shown for colloid diameters of 175 and 340 nm.

ties can act as a quencher for excited Er. This is due to the fact that the first overtone of the O—H stretch vibration is resonant with the $^4I_{13/2} \rightarrow {}^4I_{15/2}$ transition in Er^{3+}. For low quencher concentration, the decay rate can be written as

$$W_{\text{tot}} = W_r + W_i + 8\pi C_{\text{Er-Er}}[\text{Er}][Q] \tag{20}$$

with W_r as the radiative rate, W_i as the internal nonradiative rate, e.g., due to multiphonon relaxation or coupling to defects, $C_{\text{Er-Er}}$ as a coupling constant, and [Er] and [Q] as the Er and quencher concentration, respectively. The dashed lines in Fig. 34 are fits using Eq. (20), assuming the same slope but a different offset for each type of sample. The fact that both data sets can be described by the same slope indicates that the quencher concentration in 175 nm and 340 nm colloids is the same, which is expected, as the fabrication procedure for the two sizes is similar. Using a typical value for $C_{\text{Er-Er}}$ from the literature $(10^{-39}\ \text{cm}^6\ \text{s}^{-1})^5$ we find a quencher concentration of 100 ppm. Assuming the dominant quencher is OH, this is a reasonable value, as the colloids were prepared in a wet-chemical reaction.

The vertical intercepts of the fits in Fig. 34 represent the Er decay rates in the absence of concentration quenching ($W_r + W_i$): they are 70.4 s^{-1} (14.2 ms) and 50.3 s^{-1} (19.9 ms) for 175 nm and 340 nm colloids, respectively, and are listed in Table VI under $W_{\text{tot}}^{\text{Er}=0}$. These rates can now be compared to calculated values of W_r that can be derived as described next.

Figure 35 shows a calculation of the local optical DOS in spherical silica colloids, calculated using a Green's function approach.[73] The factor $\epsilon(\mathbf{r})$ is included in the definition of the DOS [see Eq. (19)], making the DOS directly proportional to the radiative decay rate. Since the polarization of the emitted radiation is randomly oriented, due to the amorphous structure of the silica glass network, integration over both polarizations is done.

In Fig. 35, the local DOS is plotted for a vacuum wavelength of $\lambda_0 = 1.535\ \mu$m as a function of radial distance for the two different colloid diameters. The colloids (refractive index $n=1.45$) are surrounded by air ($n=1.00$), and the DOS is normalized to the local DOS in bulk silica (defined as $f_{1.45}=1$). As can be seen, the value of the DOS inside the colloid differs strongly between spheres of different size. Depending on the size, the DOS is smaller or larger than the DOS for bulk SiO_2. For a given size, not much variation in the DOS is observed inside the sphere. This can be explained by the fact that for both colloid sizes $2\pi r \leqslant \lambda_0/n$ (with r as the colloid radius), hence no Mie resonances are observed. Assuming that the Er ions are distributed homogeneously over the SiO_2 sphere, the effect of the sphere on the radiative rate can be calculated by integrating the DOS in Fig. 35 over the sphere volume. For a 175 nm sphere the calculation yields $f_{1.45}^i = 1.13$, while for a 340 nm sphere a value of $f_{1.45}^i = 0.74$ is found. These data are also listed in Table VI.

Using these two DOS factors, the radiative rates in the colloids can be calculated, using as input the radiative rate of Er in bulk SiO_2 ($54 \pm 10\ s^{-1}$) that we have previously determined.[74] An identical rate ($55 \pm 5\ s^{-1}$) was derived from our analysis of data by Vredenberg *et al.*,[75] described in Ref. 75. From the fact that the PL spectrum for the colloids in Fig. 33 is identical to that of the Er-implanted SiO_2 in our previous work,[74] we conclude that the local environment in both materials is similar, and that therefore the bulk decay rate of 54 s^{-1} can also be applied to the silica glass used for the colloids. Multiplying this decay rate with the DOS factors of 1.13 and 0.74 found herein gives the purely radiative

TABLE VI. Measured and calculated Er luminescence decay rates for two different colloid diameters (175 and 340 nm).

Colloid diameter	$f_{1.45}$	$W_{\text{tot}}^{\text{Er}=0}$ (s^{-1})	W_r (s^{-1})	$W_i^{\text{Er}=0}$ (s^{-1})
175 nm	1.13	70	61	9
340 nm	0.74	50	40	11

decay rate in the two types of colloids: $W_r = 61\ s^{-1}$ (175 nm spheres) and $W_r = 40\ s^{-1}$ (340 nm spheres). These data are summarized in Table VI. Using the radiative rate for Er in bulk SiO_2 and the Fuchtbauer–Ladenberg equation,[76] we can derive a peak cross section of $4.0 \times 10^{-21}\ cm^2$. This value was used to provide a cross section scale in Fig. 33.

Several conclusions can be drawn by comparing these numbers with the data in Fig. 34. First, the vertical separation between the two linear curves through the data for the two types of colloids is equal to $20 \pm 5\ s^{-1}$, which is identical to the difference between the radiative rates calculated herein ($21\ s^{-1}$). This provides clear evidence that the data can be consistently described by the DOS model. Second, subtracting for the two colloid diameters, the measured decay rate in absence of concentration quenching ($W_{tot}^{Er=0}$) from the calculated radiative rate (W_r) (see Table VI), we find the intrinsic nonradiative decay rate W_i; it amounts to 9 s^{-1} or 10 s^{-1} for the 175 nm and 340 nm colloids, respectively (see Table VI). The relative error on these values is ± 5 s^{-1} and the absolute error $\pm 10\ s^{-1}$. These values for W_i are consistent with the fact that identical intrinsic nonradiative decay rates are expected for both colloid diameters as they are fabricated in an identical way. This again shows that the data in Fig. 34 can be consistently described by the DOS model.

Finally, we determine the luminescence quantum efficiency (QE) of excited Er. Although the QE has a relatively large error bar ($\pm 10\%$–20%) due to the uncertainty in W_i, it can be concluded that (1) in the absence of concentration, quenching the QE is on the order of 80%, (2) the 175 nm colloids have larger QE than the 340 nm colloids, and (3) increasing the concentration from 0 to, e.g., 0.5 at. % reduces the QE by some 20%.

VII. RARE-EARTH DOPED POLYMER WAVEGUIDE AMPLIFIERS: OUTLOOK

A. Optically pumped rare-earth doped polymer amplifiers

1. Rare-earth doped organic complexes

As we have seen in Secs. II and III, organic cage complexes can be used to encapsulate the rare-earth ion, thereby making it dissolvable into the polymer. In this way, the rare-earth doping problem was solved. However, we also found that the optical transitions in the rare-earth ions are quenched due to coupling with vibrational overtones of C—H and O—H bonds in the complex or polymer. Deuteration of the complex reduces the quenching by a factor of 2. Still, the quantum efficiency achieved is less than 1%. It seems this is an intrinsic problem for the use of organic complexes and polymer hosts.

At the short luminescence lifetimes found, very high pump powers are required to achieve population inversion. This problem was solved by attaching a highly absorbing lissamine sensitizer to the complex. Population inversion can now be achieved at very low pump powers (~ 1 mW) in the waveguide. However, it should be noted that the gain efficiency is low, since that is determined by the internal quantum efficiency of the rare-earth ion. One problem found with the use of the lissamine sensitizer is that it exhibits photodegradation upon illumination (Sec. III D), which is thought to be the result of a photo-oxidation reaction. This problem might be solved by encapsulation of the devices, and fabrication under N_2 atmosphere to avoid O_2 contamination. Due to the high absorption of the lissamine, traditional butt–end coupling of the waveguide amplifier is not practical. The coupling scheme using a pump waveguide parallel to the signal waveguide, introduced in Sec. IV, can be used to increase the pumping efficiency in the waveguide. A pump power of ~ 1 W is needed to achieve an optical gain of 1.6 dB in the waveguide. Given this power, photostability will be a key parameter in the final choice of the used polymer.

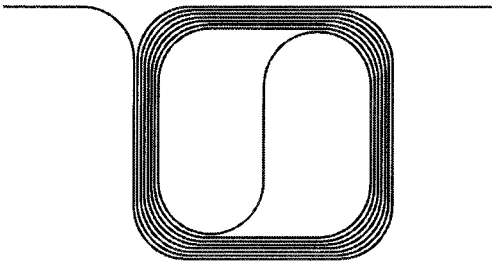

FIG. 36. Planar 15 cm long optical waveguide amplifier rolled up on an area of $\sim 16\ mm^2$. Due to the high index contrast that can be achieved using polymer technology, a small bending radius can be made.

2. Rare-earth doped silica colloids

The problem of C—H quenching can be overcome by using Er-doped silica colloids. These silica colloids can be dissolved in a polymer to form the core layer of a planar polymer waveguide amplifier. This composite material enables high gain, provided the index of the polymer can be matched accurately with that of the colloids. Yoshimura *et al.*[77] have shown that by mixing fluorinated and deuterated PMMA, the refractive index of the mixed polymer can be tuned around 1.45 with an accuracy <0.001, and that the resulting material can be used to produce low-loss optical waveguides. This combination is a promising candidate as a polymer host for Er^{3+}-doped silica sphere/polymer nanocomposite optical waveguides, and gain predictions (see Sec. V) show a very low (several mW) pump threshold for optical gain. To reduce the effect of cooperative upconversion interactions between excited Er ions, the Er concentration in the colloid must be kept below ~ 0.8 at. %. As a result, a rather long waveguide (~ 15 cm) is required to achieve reasonable gain (8.7 dB at 30 mW). We note that due to the large index contrast between polymer core and cladding a rather small waveguide bending radius can be achieved. Figure 36 shows a waveguide spiral geometry in which a 15 cm long waveguide is rolled up on an area of only 16 mm^2 by employing the minimum tolerable bending radius of 170 μm.

3. Alternative methods for Er incorporation

The Er ion implantation experiments have clearly demonstrated that silica colloids form an ideal host for Er. The next step would be to develop a method by which the Er could be incorporated directly using the wet-chemical pro-

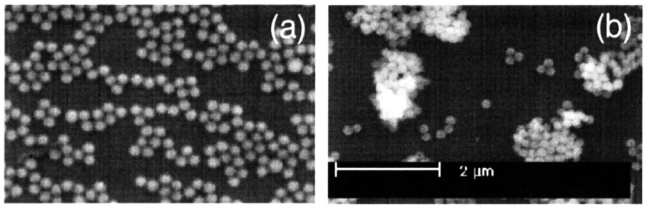

FIG. 37. SEM images of silica spheres on a Si substrate. The spheres were first deposited on a Si substrate coated with a carbon film, then one sample was used for reference (a) and one was annealed at 750 °C for 1 h (b). Finally the spheres were dissolved in ethanol using an ultrasonic bath, and deposited again on a Si substrate.

cess used to form the colloids, thus avoiding the implantation step. We have tried several approaches to achieve this. These experiments were performed on silica films, rather than colloids, using a similar chemical process as discussed in Ref. 52.

First, we have grown a 65 nm thick silica film, that was then put in a solution of $Er(NO_3)_3 \cdot 5H_2O$ and afterwards annealed at 950 °C. RBS showed indications for a small amount of Er left at or near the surface, but no PL from Er at 1.5 μm was observed. Second, we tried the use of a 3-aminopropyltriethoxysilane (APS) coupling agent. A 75 nm thick oxide film was first grown, subsequently a 75 nm thick layer was grown using the coupling agent, and next the sample was put in an $Er(NO_3)_3 \cdot 5H_2O$ solution. Again, a small Er content was measured on the film surface using RBS but no PL was observed. Mixing the APS with the Er nitrite also did not lead to the desired result. Finally, we investigated the use of N-(trimethoxysilylpropyl)-ethylenediamine, triacetic acid, trisodium salt (EDTA), a method that has previously shown to lead to the incorporation of metal ions in an acid-catalyzed sol–gel process.[54] Again, no Er-related PL was observed on these grown films.

As becomes clear from this summary, the task to find a process to incorporate Er during the wet-chemical reaction remains. Two approaches come to mind: (1) a different Er precursor such as, e.g., erbium methoxyethoxide or isopropoxide[78] may be used, or (2) an erbium (III) PMMA coating could be made around the silica colloids, that could then be covered with the pure oxide, whereupon the Er could be diffused into the colloid by thermal annealing.

4. Thermal annealing of Er colloids

As shown in Sec. V, thermal annealing is essential to optically activate the Er in the ion-implanted colloids. Even if a successful, wet-chemical process to incorporate Er were developed, thermal annealing will likely be necessary. One important question is whether annealed colloids can actually be redispersed in solution, for later incorporation in the polymer waveguide. Figure 37(b) shows a SEM image of a surface covered with colloids that were first deposited on a carbon-coated Si wafer, then annealed in a vacuum at 750 °C for 1 h, ultrasonically lifted from the substrate, and then redeposited. A reference sample that did not have the anneal treatment is shown in Fig. 37(a). Clearly, larger agglomerates of clusters are observed for the annealed material. At the present colloid size used, the size of these clusters is impractical for application in waveguides. To reduce the size of these clusters, smaller colloids could be used. Alternatively, core-shell particles could be used, that are composed of a shell that does not sinter at 750 °C or that evaporates during annealing thus isolating the colloids so that no sintering can occur.

B. Toward an electrically pumped waveguide amplifier

Recently, we, together with a group at Cambridge University, have shown 890 nm luminescence from a neodymium-doped polymer light-emitting diode (LED).[79] The active layer was a blend of poly(dioctylfluorene-co-benzothiadiazole), and a lissamine-functionalized terphenyl-based neodymium complex. It was shown that charge injection into the conducting polymer was followed by energy transfer to the sensitizer, resulting in excitation of the neodymium ion. Using this concept of energy transfer from a conjugated polymer to a sensitized rare-earth complex, it becomes possible to fabricate an electrically pumped polymer waveguide amplifier operating in the near infrared. Note that there is no conjugated polymer known that emits at these wavelengths. In order to have energy transfer from the polymer to the sensitizer, the sensitizer and conjugated polymer have to be chosen such that the emission of the polymer overlaps the absorption spectrum of the sensitizer. More details are given in Ref. 79.

It should be noted that the indium tin oxide (ITO) electrode that is standard used in polymer LEDs is not optimized for the infrared emission wavelength. For example, a 130 nm thick ITO electrode absorbs 6% of the light at 890 nm. At a wavelength of 1.5 μm, more than 80% of the light would be absorbed in such a film. Clearly, optimization of the ITO composition, or the use of alternative materials that transmit better in the infrared but still have reasonable conductivity, such as $CuAlO_2$ and $CuGaO_2$,[80,81] must be considered to improve the infrared emission intensity in these sensitized rare-earth doped polymer LEDs. For the anode, Al can be used, as it has a high reflection ($\sim$90%) at 1500 nm.

The issue of transparent conducting electrodes becomes even more important when these sensitized rare-earth doped polymers are used in an electrically pumped optical waveguide amplifier, as the interaction length with the electrode in such a device is on the order of centimeters. Such a waveguide structure consists of an active (rare-earth doped, high refractive index) waveguide core, embedded in an electrically conducting cladding layer with lower refractive index. In this geometry, it would be desirable to use thick waveguide cladding layers to minimize the interaction between the optical mode and the electrodes. At the same time, such cladding layers must be efficient electron and hole conductors, i.e., have high carrier mobilities. A hole conducting layer that may suit this requirement is N,N′-diphenyl-N,N′-bis(3-methylphenyl)-1,1′-biphenyl-4,4′-diamine (TPD) which has a hole drift mobility of 10^{-3} $cm^2/V\,s$.[82] It is more difficult to find a good electron conducting polymer, although some promising results have been reported for 1,2,3-oxadiazole derivative (PBD) (Refs. 83 and 84) and poly(phenyl quinoxaline) (PPQ).[85] However, all these

materials have been used in very thin layers of ~100 nm. For a typical cladding layer thickness of 1 μm, the operating voltage of an electrically pumped waveguide amplifier will be higher than that for the LED of Ref. 79. Therefore, more detailed studies of the optical properties of electron and hole conducting layers are required to further optimize the polymer waveguide amplifier device design.

VIII. CONCLUSIONS

Rare-earth doped polydentate hemispherand organic cage complexes show a broad PL spectrum at room temperature. The luminescence lifetime of the rare-earth ions is short, in the order of μs, much shorter than the estimated radiative lifetime of several 250 μs for Nd^{3+} and 4 ms for Er^{3+}. This short luminescence lifetime is attributed to the presence of C—H or O—H groups in the complex or the polymer host. The rare-earth ion can be excited directly in the $4f$ manifold, or indirectly via the aromatic rings of the complex or a covalently bonded highly absorbing sensitizer. Optical gain calculations show that Er^{3+}-doped organic complexes, when dissolved in a polymer channel waveguide, show net optical amplification for a pump power as low as 1.4 mW and a typical differential gain of 1.7 dB/cm.

It is shown that the excitation efficiency upon excitation via the sensitizer is four orders of magnitude higher than for direct excitation. Good quality optical waveguides can be spincoated with optical losses for the undoped polycarbonate waveguide of <0.05 dB/cm at 1060 nm and 0.08 dB/cm at 1340 nm. The lissamine sensitizer shows photobleaching, resulting in an initial increase in intensity due to concentration quenching and self-absorption. The Nd^{3+} luminescence intensity shows no initial increase, which suggests that concentration quenching has no effect on the Nd^{3+} luminescence.

We have introduced an optical waveguide system, consisting of two closely spaced parallel waveguides, that can be used to optimize the pumping of planar waveguide amplifiers. Calculations show that light coupled into the pump guide will gradually couple to the signal guide, resulting in a more efficient power distribution along the signal guide.

Room-temperature luminescence at 1.5 μm from Er-implanted silica colloidal spheres was observed. The luminescence lifetime of Er is about 17 ms, and the quantum efficiency is estimated to be 80%. Thermal annealing at 750 °C is required to optimize the luminescence intensity. The colloids can be embedded in a polymer to achieve an optically active nanocomposite waveguide layer. It is shown that the refractive index of the polymer and colloids must be nearly matched, and that the size of the spheres has to be relatively small in order to have tolerable scattering losses. Calculations of the optical gain that can be achieved with these Er-doped silica sphere/polymer nanocomposite optical waveguide amplifiers show a maximum gain of 12 dB for a 15 cm long amplifier and an Er concentration of 0.8 at. %. This 15 cm long waveguide can be ''rolled up'' on an area of only 16 mm^2.

The decay rate at 1.5 μm of Er ions implanted into a 100 nm thick SiO_2 film on Si, made using a wet-chemical process, was measured with and without liquids with different refractive index in contact with the film. The observed increase in decay rate with refractive index is explained by a change in the local optical DOS at the position of the Er. By comparing a calculation of the local DOS with the measured decay rates, the radiative (69 s^{-1}) and nonradiative (115 s^{-1}) components were distinguished. Using a calculation of the DOS for a sphere in air and the radiative decay rate determined for a SiO_2 film, the contribution of radiative and nonradiative decay to the total decay rates of Er-implanted SiO_2 spheres with a diameter of 340 nm, and 175 nm was determined.

Finally an outlook is given on the requirements for the material properties for optically and electrically excited polymer waveguide amplifiers.

ACKNOWLEDGMENTS

This work was part of the research program of the Foundation of Research on Matter (FOM) and was made possible by financial support from the Dutch Technology Foundation (STW), IOP Electro-Optics Program of the Ministry of Economic Affairs, and the ESPRIT program (SCOOP) of the European Community. It is a great pleasure to acknowledge all co-workers who have contributed to the work described in this review article: T. van Dillen, M. de Dood, A. Tip, P. Kik, A. Moroz, and D. Vossen at FOM-AMOLF, C. van Kats at the University of Utrecht, B. Hams at JDS-Uniphase, F. Geurts and H. Lamers at Akzo-Nobel, M. O. Wolbers, F. Steemers, and L. Grave, University of Twente, and M. Werts at the University of Amsterdam.

APPENDIX A

From the reciprocity theorem,[45] it follows that:

$$\left.\begin{aligned}\gamma_a &= \beta_a + \frac{K_{aa} - CK_{ba}}{1-C^2}\\ \gamma_b &= \beta_b + \frac{K_{bb} - CK_{ab}}{1-C^2}\end{aligned}\right\} \quad \text{modified propagation constant}$$

$$\left.\begin{aligned}k_{ab} &= \frac{K_{ab} - CK_{bb}}{1-C^2}\\ k_{ba} &= \frac{K_{ba} - CK_{aa}}{1-C^2}\end{aligned}\right\} \quad \text{modified coupling constants} \qquad (21)$$

$$C = (C_{ab} + C_{ba})/2,$$

with the conventional propagation constant β and coupling constant K_{ab}, and K_{ba} given by

$$\beta_{a,b} = \frac{2\pi(n_{a,b} + k_{a,b})}{\lambda}$$

$$K_{ab} = \frac{\omega}{4}\int\int \epsilon^b(x,y)[E_t^a \cdot E_t^b - E_z^a \cdot E_z^b]dxdy, \qquad (22)$$

$$K_{ba} = \frac{\omega}{4}\int\int \epsilon^a(x,y)[E_t^b \cdot E_t^a - E_z^b \cdot E_z^a]dxdy$$

where

$$\epsilon^{a,b}(x,y) = \epsilon(x,y) - \epsilon^{a,b}(x,y).$$

Here, $n_{a,b}$ is the real part of the refractive index, $k_{a,b}$ is the imaginary part of the refractive index, $\epsilon(x,y)$ is the permittivity function for the complete waveguide system, and $\epsilon^{a,b}(x,y)$ the permittivity function for the isolated waveguides A and B.

APPENDIX B

The lissamine is excited from the singlet ground state (S_0) (see Fig. 10) into the excited singlet state (S_1) at a pump rate W_p, after which it can decay to the ground state at a rate W_{s1}, or to the triplet state (Table IV gives the values for the different rates used in the optical gain calculation (T) via intersystem crossing at a rate W_{isc}. From the triplet state, it can then decay to the ground state radiatively at a rate W_{s2}, or nonradiatively by transferring its energy to the neodymium ion via Dexter energy transfer at a rate W_{et}. After the energy transfer process, the neodymium will be in the $^4F_{9/2}$ and $^4S_{3/2}$ level, from which it decays rapidly to the luminescent $^4F_{3/2}$ state. We assume that the decay between adjacent levels is very fast, so that effectively the neodymium is excited directly into the $^4F_{3/2}$ level (N_4). We also assume rapid decay from the N_1, and N_2 levels to the ground state. The rate equations can then be written as

$$\begin{aligned}
\frac{dS_0}{dt} &= -W_p S_0 + W_{s1} S_1 + W_{s2} T + W_{et} T N_0 \\
\frac{dS_1}{dt} &= +W_p S_0 - W_{s1} S_1 - W_{\text{isc}} S_1 \\
\frac{dT}{dt} &= +W_{\text{isc}} S_1 - W_{s2} T - W_{et} T N_0 \\
\frac{dN_0}{dt} &= -W_{et} T N_0 + W_{40} N_4 \\
\frac{dN_4}{dt} &= +W_{et} T N_0 - W_{40} N_4 .
\end{aligned} \tag{23}$$

The Nd population in N_4 is derived by solving these rate equations for steady state. The total concentration of lissamine is equal to the Nd concentration, i.e. $S_0+S_1+T=N_0+N_4=N$. The fraction of excited Nd is given by: $f=N_4/N$. The values of the different rate constants are given in Table IV and have been derived from spectroscopic measurements described in Section III except from W_{et}, which is estimated from oxygen quenching experiments,[22] and W_{s2} which is an estimate based on typical triplet state lifetimes.

[1] For a review see: P. G. Kik and A. Polman, MRS Bull. **23**, 48 (1998).
[2] S. Tang, B. Li, D. An, L. Sun, Z. Shi, and R. T. Chen, Proc. SPIE **4225**, 400 (2001).
[3] For a review see: L. Eldada and L. W. Shacklette, IEEE J. Sel. Top. Quantum Electron. **6**, 54 (2000).
[4] For a review see: L. Eldada and L. W. Shacklette, IEEE J. Sel. Top. Quantum Electron. **11**, 54 (2000).
[5] V. P. Gapontsev, A. A. Izyneev, Y. E. Sverchov, and M. R. Syrtlanov, Sov. J. Quantum Electron. **11**, 1101 (1981).
[6] A. J. Bruce, W. A. Reed, A. E. Neeves, L. R. Copeland, W. H. Grodkiewicz, and A. Lidgard, Mater. Res. Soc. Symp. Proc. **244**, 157 (1992).
[7] Yingchao Yan, A. J. Faber, and H. de Waal, J. Non-Cryst. Solids **181**, 283 (1995).
[8] M. P. Oude Wolbers, F. C. J. M. van Veggel, B. H. M. Snellink-Ruël, J. W. Hofstraat, F. A. J. Geurts, and D. N. Reinhoudt, J. Am. Chem. Soc. **119**, 138 (1997).
[9] J. N. Sandoe, P. H. Sarkies, and S. Parke, J. Phys. D **5**, 1788 (1972).
[10] A. Polman, D. C. Jacobson, D. J. Eaglesham, R. C. Kistler, and J. M. Poate, J. Appl. Phys. **70**, 3778 (1991).
[11] E. Snoeks, G. N. van den Hoven, and A. Polman, J. Appl. Phys. **73**, 8179 (1993).
[12] G. N. van den Hoven, E. Snoeks, A. Polman, J. M. W. van Uffelen, Y. S. Oei, and M. K. Smit, Appl. Phys. Lett. **62**, 3065 (1993).
[13] W. J. Miniscalco, J. Lightwave Technol. **9**, 234 (1991).
[14] G. N. van den Hoven, E. Snoeks, J. A. van der Elsken, C. van Dam, J. M. W. van Uffelen, and M. K. Smit, Appl. Opt. **36**, 3338 (1996).
[15] M. P. Oude Wolbers, Ph.D. thesis, University of Twente, 1997.
[16] V. L. Ermolaev and E. B. Sveshnikova, Russ. Chem. Rev. **63**, 905 (1994).
[17] C. K. Jørgensen, *Lasers and Excited States of Rare Earths* (Springer, New York, 1977).
[18] G. Nykolak, M. Haner, P. C. Becker, J. Schmulovich, and Y. H. Wong, IEEE Photonics Technol. Lett. **5**, 1014 (1993).
[19] G. N. van den Hoven, E. Snoeks, A. Polman, C. van Dam, J. M. W. van Uffelen, and M. K. Smit, J. Appl. Phys. **79**, 1258 (1996).
[20] L. H. Slooff, A. Polman, M. P. Oude Wolbers, F. C. J. M. van Veggel, D. N. Reinhoudt, and J. W. Hofstraat, J. Appl. Phys. **83**, 497 (1998).
[21] G. Stein and E. Würzberg, J. Chem. Phys. **62**, 208 (1975).
[22] S. I. Klink, Ph.D. thesis, University of Twente, Enschede, The Netherlands (2000).
[23] I. B. Berlman, *Handbook of Fluorescence Spectra of Aromatic Molecules* (Academic, New York, 1971).
[24] R. H. Woudenberg, and T. O. Boonstra, International Patent No. WO 9838237 3 September 1998.
[25] M. J. Weber, Phys. Rev. **171**, 283 (1968).
[26] H. P. Weber, F. A. Dunn, and W. N. Leibolt, Appl. Opt. **12**, 755 (1973).
[27] M. G. Kucherenko and M. P. Mel'nik, J. Appl. Spectrosc. **60**, 344 (1994).
[28] F. Wilkinson, W. P. Helman, and A. B. Ross, J. Phys. Chem. Ref. Data **22**, 113 (1993).
[29] It is assumed that the quenching by O_2 is a diffusion controlled mechanism at a rate $kq=1010\ \text{M}^{-1}\ \text{s}^{-1}$, for a typical O_2 concentration in solution the total quenching rate is $kq[O_2]\approx 107\ \text{s}^{-1}$.
[30] E. van der Tol, Ph.D. thesis, University of Amsterdam, Amsterdam, The Netherlands, 1998.
[31] D. L. Dexter, J. Chem. Phys. **21**, 836 (1953).
[32] M. H. V. Werts, J. W. Hofstraat, F. A. J. Geurts, and J. W. Verhoeven, Chem. Phys. Lett. **276**, 196 (1998).
[33] R. P. Wayne, *Principles and Applications of Photochemistry* (Oxford University Press, Oxford, 1998).
[34] T. Förster and E. Koning, Z. Elektrochem. **61**, 344 (1957).
[35] E. G. McRae and M. Kasha, J. Chem. Phys. **28**, 721 (1958).
[36] R. W. Chambers, T. Kijiwara, and D. R. Kearns, J. Phys. Chem. **78**, 380 (1974).
[37] S. A. Ahmed, Z.W. Zang, K. M. Yoo, M. A. Ali, and R. R. Alfano, Appl. Opt. **33**, 2746 (1994).
[38] S. Tobita, M. Arakawa, and I. Tanaka, J. Chem. Phys. **88**, 2697 (1984).
[39] S. Tobita, M. Arakawa, and I. Tanaka, J. Chem. Phys. **89**, 5649 (1985).
[40] M. H. V. Werts, J. W. Hofstraat, F. A. J. Geurts, and J. W. Verhoeven, Chem. Phys. Lett. **276**, 196 (1997).
[41] M. Kubista, J. Nygren, A. Elbergali, and R. Sjöback, Crit. Rev. Anal. Chem. **29**, 1 (1999).
[42] L. H. Slooff, A. Polman, S. I. Klink, G. A. Hebbink, L. Grave, F. C. J. M. van Veggel, D. N. Reinhoudt, and J. W. Hofstraat, Opt. Mater. **14**, 101 (2000).
[43] H. Kogelnik, in *Integrated Optics*, edited by T. Tamir, 2nd ed. (Springer, Berlin, 1979), Sec. 2.
[44] D. Marcuse, *Theory of Dielectric Optical Waveguides*, 2nd ed. (Academic, Boston, 1991).
[45] S.-L. Chuang, J. Lightwave Technol. **5**, 5 (1987).
[46] S.-L. Chuang, *Physics of Optoelectronic Devices* (Wiley, New York, 1995).
[47] S. Hongyuan, L. Tianguan, Z. Ruirong, Z. Yuping, Y. Guijang, H. Chenghui, L. Hong, and Z. Ahengdong, IEEE J. Quantum Electron. **25**, 144 (1989).
[48] H. Dai, O. M. Stafsudd, and B. Dunn, Appl. Opt. **30**, 4330 (1991).
[49] A. Sennaronglu, Opt. Commun. **164**, 191 (1999).
[50] S. Lin, J. Feuerstein, and A. R. Mickelson, J. Appl. Phys. **79**, 2868 (1996).
[51] A. van Blaaderen and A. Vrij, Langmuir **8**, 2921 (1993).
[52] D. L. J. Vossen, M. J. A. de Dood, T. van Dillen, L. H. Slooff, C. M. van

Kats, T. Zijlstra, E. van der Drift, A. Polman, and A. van Blaaderen, Adv. Mater. **12**, 1434 (2000).
[53] X. Fan, M. Wang, and G. Xiong, Mater. Sci. Eng., B **21**, 55 (1993).
[54] P. Tien and L.-K. Chau, Chem. Mater. **11**, 2141 (1999).
[55] E. Snoeks, P. G. Kik, and A. Polman, Opt. Mater. **5**, 159 (1996).
[56] W. Barnes, J. Mod. Opt. **45**, 661 (1998).
[57] E. Snoeks, A. Lagendijk, and A. Polman, Phys. Rev. Lett. **74**, 2459 (1995).
[58] F. Auzel, J. Lumin. **45**, 341 (1990).
[59] P. Blixt, J. Nilsson, T. Carlnäs, and B. Jaskorzynska, IEEE Photonics Technol. Lett. **3**, 996 (1991).
[60] C. C. Ye, P. R. Morkel, E. R. Taylor, and D. N. Payne, in *Proceedings of the 19th European Conference on Optical Communication*, Montreux, Switzerland, 12–16 Sept., 1993, Vol. 2, p. 73–76.
[61] E. Snoeks, G. N. van den Hoven, A. Polman, B. Hendriksen, M. B. J. Diemeer, and F. Priolo, J. Opt. Soc. Am. B **12**, 1468 (1995).
[62] C. G. Atkins, J. R. Armitage, R. Wyatt, B. J. Ainslie, and S. P. Craig-Ryan, Opt. Commun. **73**, 217 (1989).
[63] R. S. Quimby, W. J. Miniscalco, and B. Thompson, Proc. SPIE **1789**, 50 (1993).
[64] L. H. Slooff, M. J. A. de Dood, A. van Blaaderen, and A. Polman, Appl. Phys. Lett. **76**, 3682 (2000).
[65] M. Kai, O. Painter, and K. H. Vahala, Phys. Rev. Lett. **85**, 74 (2000).
[66] L. Cognolato, C. De Bernardi, M. Ferraris, A. Gnazzo, S. Morasca, and D. Scarano, CSELT Tech. Rep. **XIX**, 277 (1991).
[67] E. Desurvire, *Erbium-Doped Fiber Amplifiers* (Wiley, New York, 1994).
[68] L. H. Slooff, M. J. A. de Dood, A. van Blaaderen, and A. Polman, J. Non-Cryst. Solids **296**, 158 (2001).
[69] Typical order of magnitude, see e.g., G. N. van den Hoven, A. Polman, C. van Dam, J. W. M. van Uffelen, and M. K. Smit, Appl. Phys. Lett. **68**, 1886 (1996).
[70] J. C. Wright, in *Radiationless Processes in Molecules and Condensed Phases*, edited by F. K. Fong (Springer, Heidelberg, 1976).
[71] H. C. Chow and R. C. Powell, Phys. Rev. B **21**, 3785 (1980).
[72] See for a review: W. L. Barnes, J. Mod. Opt. **4**, 661 (1998).
[73] A. Moroz, Europhys. Lett. **46**, 419 (1999).
[74] M. J. A. de Dood, L. H. Slooff, A. Moroz, A. van Blaaderen, and A. Polman, Phys. Rev. A **64**, 033807 (2001).
[75] A. M. Vredenberg, N. E. J. Hunt, E. F. Schubert, D. C. Jacobson, J. M. Poate, and G. J. Zydzik, Phys. Rev. Lett. **71**, 517 (1993).
[76] $W_{\mathrm{rad}}=8\pi n^2/c^2\int v^2\sigma(v)\mathbf{d}v$, where n is the host refractive index ($n=1.45$), c is the speed of light, and v is the optical frequency of the transition involved.
[77] R. Yishimura, M. Hikita, S. Tomaru, and S. Imamura, J. Lightwave Technol. **16**, 1030 (1998).
[78] G. Milova, S. I. Najafi, A. Skirtach, D. Simkin, and M. P. Andrews, Proc. Soc. Photo-Opt. Instrum. Eng. **2997**, 90 (1997).
[79] L. H. Slooff, A. Polman, F. Cacialli, R. H. Friend, G. A. Hebbink, F. C. J. M. van Veggel, D. N. Reinhoudt, Appl. Phys. Lett. **78**, 2122 (2001).
[80] E. Stauber, J. D. Perkins, P. A. Parilla, and D. S. Ginley, Electrochem. Solid-State Lett. **2**, 654 (1999).
[81] H. Kawazoe, H. Yanagi, K. Ueda, and H. Hosono, MRS Bull. **25**, 28 (2000).
[82] J. Kido, H. Hayase, K. Hongawa, and K. Nagai, Appl. Phys. Lett. **65**, 2124 (1994).
[83] C. Adachi, K. Nagai, and S. Saito, Appl. Phys. Lett. **55**, 1489 (1989).
[84] C. Adachi, K. Nagai, and S. Saito, Appl. Phys. Lett. **57**, 531 (1990).
[85] D. O'Brien, M. S. Weaver, D. G. Lidzey, and D. C. Bradley, Appl. Phys. Lett. **69**, 881 (1996).